

INVESTIGATION OF SURFACE ANGLE EFFECTS ON SCARF JOINT
CONFIGURATIONS FOR FRICTION STIR WELDED ALUMINUM ALLOY
6061-T6511.

By

Henry Wright Gunner

Thesis

Submitted to the Faculty of the
Graduate School of Vanderbilt University
in partial fulfillment of the requirements
for the degree of

MASTER OF SCIENCE

in

Mechanical Engineering

May 13, 2022

Nashville, Tennessee

Approved:

Alvin M. Strauss, Ph.D.

Kenneth R. Pence, Ph.D.

ACKNOWLEDGMENTS

I would like to thank my girlfriend Tori for her constant love and support, which helps me to achieve all which I set out to accomplish. I would like to thank my mother Patricia and my father Geoffrey, as well as my sisters Alexandra, Elizabeth, and Violet, for their loyalty and love. To all of you, I know that if I ever stumble I will be caught, and this makes walking forward all the easier.

I would like to give the greatest gratitude to Dr. Alvin Strauss for accepting me into this position, and for his insight and mentorship during my development as a graduate student. To Dr. Ken Pence, I would also like to express my gratitude for your assistance in completing this thesis, and for agreeing to be my second reader. I would like to thank my lab-mates Connor Strawn, Lucas Wilkins, Braden Terry, and Austen Shelton for their openness to hearing my ideas, and for an unfailing willingness to help me in the process of producing this thesis. In many instances your feedback, suggestions, and well-timed puns were instrumental to my completion of it. I extend the same thank you to Benjamin Snyder, who did not let his status as an alumnus prevent him from contributing his time and positivity. I would like to thank Phil Davis for making available his broad knowledge of machining and fabricating, and his enthusiasm for running. I would also like to thank Mark Thelen for his assistance with the tensile testing of my samples.

Lastly, I would like to thank Vanderbilt University and the NASA Tennessee Space Grant Consortium for supplying the necessary financial support for me to both conduct research and continue academic growth through pursuit of this degree.

TABLE OF CONTENTS

	Page
ACKNOWLEDGMENTS	ii
LIST OF TABLES	v
LIST OF FIGURES	vi
LIST OF ABBREVIATIONS	viii
1 Introduction	1
1.1 Process Overview	1
1.2 Tool Role and Properties	3
1.3 General Process Parameters	3
1.4 Microstructure Zones and Terminology	3
1.5 Joint Configurations	4
2 Background	6
2.1 Literature Review	6
3 Experiment	11
3.1 Motivation for Current Study	11
3.2 Materials	11
3.3 Welding Machine Operation and Force Data Collection	13
3.4 Weld Parameters and Tooling	14
3.5 Temperature Data Collection	16
3.6 Final Experimental Setup	17
4 Testing and Preparation	19
4.1 Sample Preparation	19
4.2 Tensile Testing	20
5 Results	22
5.1 Z-Force Results	22
5.2 Spindle Torque Results	26
5.3 Temperature Results	29

5.4	Tensile Testing Results	34
5.4.1	Large (60° to 80°) Scarf Angle Results and Discussion	35
5.4.2	Small (40° to 50°) Scarf Angle Results and Discussion	37
5.4.3	Comparison With Study by Sethi et al.	38
5.5	Fractography Analysis	39
6	Conclusions	44
7	Future Work	47
	References	48
A	Appendix	50

LIST OF TABLES

Table		Page
5.1	Average UTS, standard deviation, and coefficient of variation of all TAS and TRS scarf welds.	36
5.2	Tool geometry and process parameters used by Sethi et al. and current study. Appropriate values converted to imperial units for direct comparison.	39
A.1	Tensile test dog bone dimensions.	58
A.2	Pre-weld lengths of all weld samples.	59

LIST OF FIGURES

Figure	Page
1.1 Friction stir welding process material zones and tool configuration. Figure adapted and annotated from TWI [7].	2
2.1 Original figure of joint geometry utilized by Kumar et al. [14]	6
2.2 Original figure of joint geometry utilized by Acharya et al. [13]	7
2.3 Generalized form of scarf joint geometry, displaying both the TAS and TRS configurations.	8
3.1 TRS 70° and TAS 40° sample pairs as examples of finished weld pieces.	12
3.2 TRS 70° and TAS 40° sample pairs, inserted together to display interaction of complimentary faying surfaces.	12
3.3 VUWAL converted Milwaukee Model K manual mill FSW welding machine.	14
3.4 FSW tool selected for this thesis, featuring a scrolled shoulder and threaded pin. There is some aluminum embedded in the threads and scrolls, but this does not impair function as under operating conditions any material on the tool surface is plasticized.	15
3.5 Thermocouple mounting and alignment with respect to a cross section perpendicular to the tool traversal direction. Example is provided in the TAS Configuration.	16
3.6 Thermocouple positions in weld apparatus.	17
3.7 Experiment setup for all conducted welds.	18
4.1 Positions from which tensile testing samples were extracted. Dotted lines represent the cuts made to create the dog bones after the weld pieces were slotted with $\frac{1}{4}$ -in slots.	19
4.2 Instron tensile tester used for determining sample strength properties.	21
5.1 TAS configuration: z-forces vs Time for all welds.	23
5.2 TRS configuration: z-forces vs Time for all welds.	24
5.3 Average z-Force for all TAS and TRS welds on the time interval t = 120 s to t = 200 s plotted versus scarf angle.	26
5.4 TAS configuration: Spindle Torque vs Time.	27
5.5 TRS configuration: Spindle Torque vs Time.	28
5.6 Average Spindle Torque vs Scarf Angle for all welds.	29
5.7 Shoulder contact area as a function of scarf angle, displayed for both the bottom and top scarf plates.	30
5.8 Butt weld temperature results	30
5.9 70° and 80° scarf weld temperature results.	31
5.10 50° and 60° scarf weld temperature results.	31
5.11 40° and 45° scarf weld temperature results.	32
5.12 Maximum AS and RS temperatures for all TAS welds vs Scarf Angle.	33

5.13	Maximum AS and RS Temperatures for all TRS welds vs. Scarf Angle. .	34
5.14	Average UTS of all TAS and TRS welds plotted versus scarf angle. Error bars represent the standard deviation of each weld's five tensile samples.	35
5.15	Examples of fractures observed for each of the conducted welds. Samples were selected to best reflect the fracture modes of their respective weld sets.	41
5.16	Close up imaging of the TRS 45° and TRS 40° joint failures.	43
A.1	Raw Load and Extension data from Tensile Testing for the TRS 40° weld samples	51
A.2	Raw Load and Extension data from Tensile Testing for the TAS 40° weld samples	51
A.3	Raw Load and Extension data from Tensile Testing for the TRS 45° weld samples	52
A.4	Raw Load and Extension data from Tensile Testing for the TAS 45° weld samples	52
A.5	Raw Load and Extension data from Tensile Testing for the TRS 50° weld samples	53
A.6	Raw Load and Extension data from Tensile Testing for the TRS 50° weld samples	53
A.7	Raw Load and Extension data from Tensile Testing for the TRS 60° weld samples	54
A.8	Raw Load and Extension data from Tensile Testing for the TAS 60° weld samples	54
A.9	Raw Load and Extension data from Tensile Testing for the TRS 70° weld samples	55
A.10	Raw Load and Extension data from Tensile Testing for the TAS 70° weld samples	55
A.11	Raw Load and Extension data from Tensile Testing for the TRS 80° weld samples	56
A.12	Raw Load and Extension data from Tensile Testing for the TAS 80° weld samples	56
A.13	Raw Load and Extension data from Tensile Testing for the butt weld samples	57

LIST OF ABBREVIATIONS

AA	aluminum alloy
AS	advancing side
DAQ	data acquisition
DBL	double lap butt joint
FSE	friction stir extrusion
FSW	friction stir welding
HAZ	heat affected zone
IPM	inches per minute
RS	retreating side
SZ	stir zone
TAS	top on advancing side
TMAZ	thermo-mechanically affected zone
TRS	top on retreating side
UTS	ultimate tensile strength
VUWAL	Vanderbilt Automation and Welding Laboratory

CHAPTER 1

Introduction

1.1 Process Overview

Friction Stir Welding (FSW) is a solid state joining process invented by Thomas et al. [1] in 1991 at TWI. The process was initially developed to allow for welding of aluminum alloys, which are difficult to weld using other welding techniques [1]. FSW has also been utilized to join a multitude of other materials such as magnesium, steel, titanium, copper, and even some plastics [2]. It can be utilized for the joining of dissimilar metals; and in this respect it is chiefly used for joining aluminum to other metals and for joining different alloys of aluminum [3]. Due to its effectiveness at joining aluminum FSW has been adopted by many aluminum-heavy industries, specifically the automotive, aerospace, and marine industries [4].

Operating temperatures for FSW allow the material to be readily plasticized but do not approach material melting temperatures, allowing for it to remain in a solid phase. This protects FSW joints from typical re-solidification defects such as porosity, embrittlement, formation of second phases and heat cracking [5]; all of which are common to fusion welding techniques such as arc welding or laser welding [4]. Because of this, FSW joints display better strength and hardness properties compared to fusion welded joints and are also extremely reproducible lending themselves to automated production [4]. The process can also be considered a “green” technology due to low energy consumption and environmental friendliness [1].

The FSW process consists of a rotating, non-consumable tool being inserted into the material, and then traversed along the weld seam. The downward pressure of the tool increases friction between the tool and the material inducing frictional heating. Shear between the tool surface and the material also contributes to heat generation. Both of these

mechanisms cause an increase in temperature until the material is plasticized, at which point the tool acts to “stir” the material along the seam. FSW is an asymmetrical process, and so distinctions must be made between the sides of the joint and tool. The side of the weld on which the tangential velocity vector of the tool is parallel to its traversal direction is called the advancing side (AS), while the side on which these vectors are anti-aligned is called the retreating side (RS), as displayed in Figure 1.1. Due to this vector alignment, the AS of the weld experiences a larger local tool velocity than the RS, which in turn causes greater heat production by the tool on the AS compared to the RS. Additionally, the edge of the tool at the front of its traversal is the leading edge, and the edge at the back is called the trailing edge. As the tool traverses, material is deposited from the leading edge to the trailing edge, which results in the formation of “onion rings” in the weld seam [5, 6]. Material is also extruded from the RS towards the AS at the trailing edge, with consolidation of the material occurring behind the tool [2].

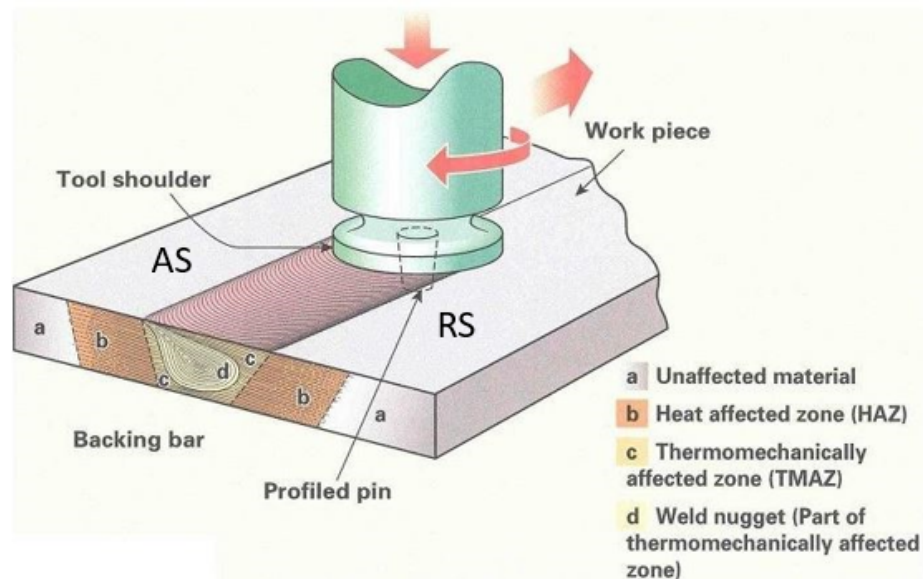


Figure 1.1: Friction stir welding process material zones and tool configuration. Figure adapted and annotated from TWI [7].

1.2 Tool Role and Properties

The tool consists of a pin and shoulder, with the pin serving a primary role in plastic deformation and mixing of the material, and the shoulder providing the process forging pressure by containing plasticized material [6]. The majority of the process heat is generated by the shoulder, but the pin also contributes to heat generation [6]. The geometry of the tool can have an extreme influence on performance of the process by impacting heat transfer and material transport. There are a variety of pin geometries available, including cylindrical, tapered-cylindrical, square and triangular pins [8]. In addition, these surfaces can also be threaded, fluted, or smooth [8]. In general, threaded and fluted pins facilitate material mixing which improves weld strength and ductility in comparison to smooth pins [8].

The shoulder can also have geometric variations such as being convex or concave and can be inscribed with scroll or groove features which improve stirring of the parent material [9]. Shoulder diameter is typically 2.5 to 3 times the plate thickness for best performance [10]. The results of Elnabi et al. [11] reported that the ratio of shoulder diameter to pin diameter has a significant impact on ductility with a confidence interval of 99%, and that a shoulder diameter to plate thickness ratio of about 3 was optimal [11].

1.3 General Process Parameters

Primary process parameters to consider for FSW are traversal speed, rotation speed, plunge depth (the depth to which the tool is inserted into the material), tool tilt angle (with respect to the vertical), and tool offset (towards either the advancing or retreating side of the weld). Process parameters dictate the performance of welds but must vary according to the material properties of the base material. For this reason, operating windows for proper parameter values are uniquely established for many materials.

1.4 Microstructure Zones and Terminology

FSW produces distinct zones in the welded material which have inherent microstructural and mechanical properties. As shown in Figure 1.1 these are the heat affected zone (HAZ),

thermo-mechanically affected zone (TMAZ), and the weld nugget (which is also referred to as the stir zone (SZ)). The nugget is characterized by fine equiaxed grains due to severe plastic deformation causing grain refinement [2]. The TMAZ experiences some plastic deformation and high temperatures, which leads to partial grain refinement in some areas and a general reduction in grain size in comparison to the base material [2]. The HAZ does not experience deformation and is only affected by heat generation. It is characterized by large grains due to grain growth caused by the high temperatures experienced. These zones exhibit different mechanical properties (ultimate tensile strength, ductility and hardness) than the base material, but overall there is much better recovery of base material properties for FSW welds compared to fusion welding technologies [2]. In terms of comparative strength the HAZ is the weakest zone, and so joint failure typically occurs in this zone close to the TMAZ [2]. The HAZ and TMAZ can be seen in Figure 1.1 to have a decreasing width from the top of the weld towards the bottom, which is due to a reduced effect of shoulder heating and deformation deeper in the weld [2].

1.5 Joint Configurations

The most common joint configurations for FSW are butt, lap, and T-joints [1]. These joint configurations can also be combined with mechanical interlocks to facilitate joint strength particularly in the case of joining dissimilar metals, with this derivative process being called friction stir extrusion (FSE). In FSE the softer metal is extruded into a geometrical feature of the the harder metal to form a mechanical interlock at the mating surface. An example of this is the dovetail extrusion joints exhibited by Evans et al. [12] for the joining of 6061 aluminum to steel, in which aluminum was extruded into different shaped grooves in steel plate, producing a mechanical interlock in addition to formation of intermetallic bonds to improve joint strength. In the welding of similar metals, mechanical interlocks do not present as much of an advantage, as the parent material on both sides of the weld share the same properties. However, changes in joint geometry could have an impact on joint

properties. The effects of tool geometry and weld parameters on weld outcomes have been extensively explored for a variety of materials, but there has been far less work concerning the effects of unique joint geometries on weld properties.

CHAPTER 2

Background

2.1 Literature Review

There are several studies available dealing with the efficacy of unique joint geometries. These geometries incorporate elements of both butt and lap configurations, but are primarily derivatives of the square butt configuration.

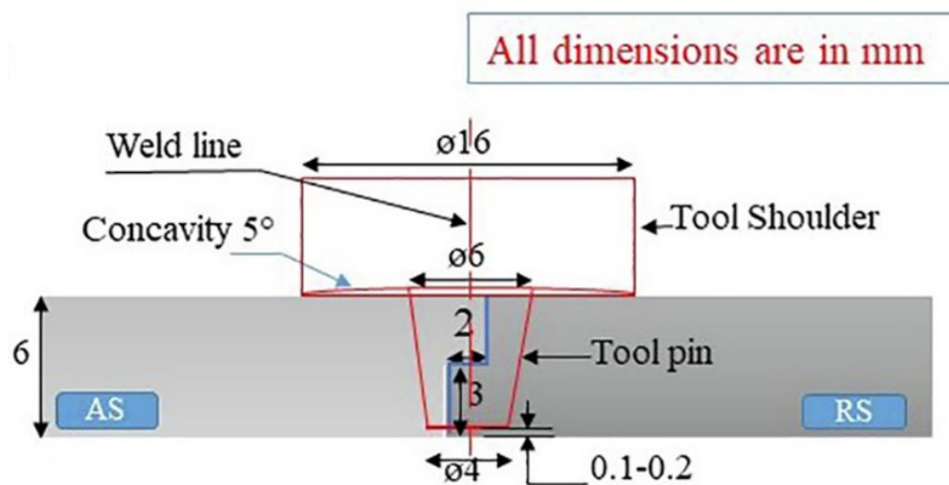


Figure 2.1: Original figure of joint geometry utilized by Kumar et al. [14]

One such joint type which has been investigated is the double-butt-lap (DBL) [13] joint. Kumar et al. [14] first investigated use of a DBL configuration in 2019, which they referred to as a “modified butt and lap joint.” Their experiment examined the use of the joint for the welding of aluminum alloy 6061-T6 and magnesium alloy AZ31B. The geometry of their joints is displayed in Figure 2.1, which shows that their geometry consisted of two symmetrical steps of equal height and width, cut into the faying surfaces of the two weld pieces. The study identified best traversal speed and rotation for optimizing weld strength (0.75 mm/s and 600 RPM respectively) [14], and reported a joint efficiency of 61% [14]. A very similar geometry, with a slight variation, was investigated by Acharya et al. [13] who christened the configuration with the name double-butt-lap joint. This name is deferred

to because Kumar et al. failed to provide their configuration with a unique name despite having primacy in its investigation. Acharya et al. investigated DBL welds of AA6061-T6 in which the weld piece features had equal widths but different heights, as displayed in Figure 2.2. The ratio of upper height (shown as UB) to lower height (shown as LB) is 4 mm to 2 mm [13]. Acharya et al. ran three welds: one conventional squared butt joint weld, one weld with the top joint feature on the advancing side (designated DBL2), and one weld with it on the retreating side (designated DBL1). With uniform weld parameters across all three welds, they reported the ultimate tensile strength (UTS) for each as 222 Mpa, 237 Mpa, and 242 Mpa respectively for the squared butt, DBL1 and DBL2 welds. This seemed to indicate that weld strength was improved by this geometry, with the DBL2 configuration having a UTS percent difference with the butt weld of 8.6%, and the DBL1 configuration having a percent difference of 3.3%.

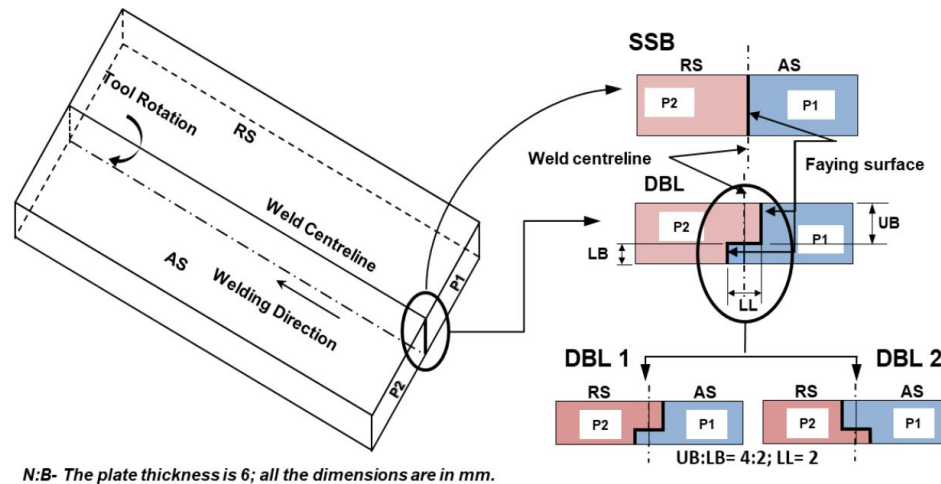


Figure 2.2: Original figure of joint geometry utilized by Acharya et al. [13]

Another joint configuration which has begun to be investigated is a scarf joint, as shown in Figure 2.3. The scarf joint consists of symmetrical chamfers of the weld piece's faying surfaces with complimentary surface angles. By convention this angle is measured with respect to the horizontal (i.e, a butt joint is considered a 90° scarf joint). However the reviewed works by Goel et al. [15] and Sethi et al. [16, 17] do not provide naming conventions for joint orientation between the top and bottom scarf surfaces and the weld advancing and

retreating sides. Due to this, the following naming conventions are introduced: the top on advancing side (TAS) configuration is defined as the configuration in which the top scarf surface is located on the advancing side, and the top on retreating side (TRS) configuration is defined as the configuration in which the top scarf surface is located on the retreating side. These geometries are also visible in Figure 2.3.

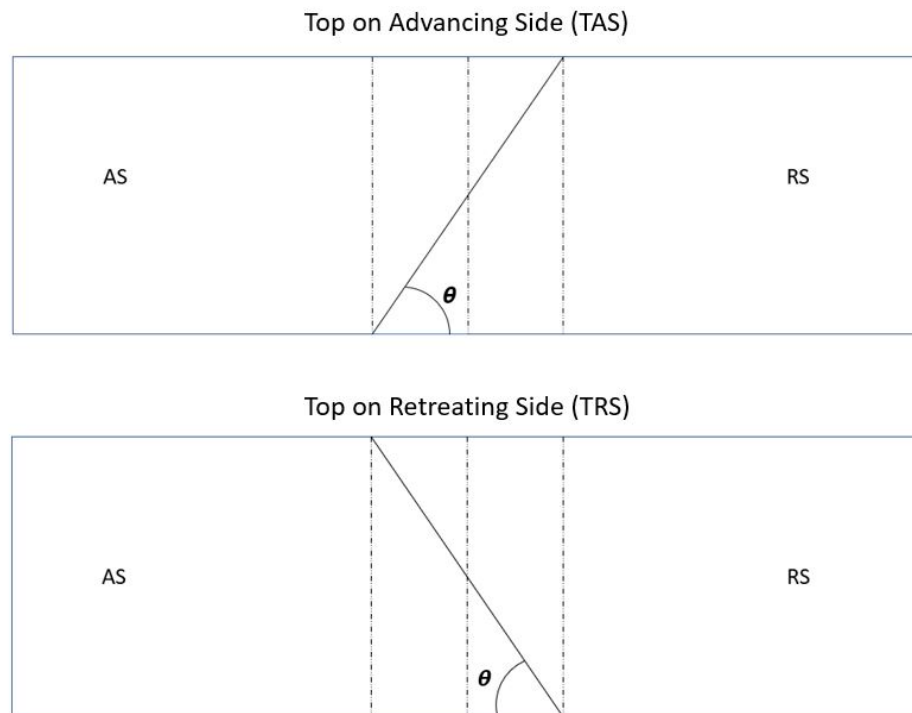


Figure 2.3: Generalized form of scarf joint geometry, displaying both the TAS and TRS configurations.

Goel et al. [15] are credited with the conception of the scarf joint weld geometry in 2018. Their experiment was primarily a pin geometry study, consisting of welds conducted with five different smooth pin geometries (cylindrical, cylindrical-tapered, triangular, square, and hexagonal), with constant process parameters; and, with each pin type used to join one 26° scarf joint in the TAS configuration. Additionally, each pin was also used to join a butt joint as a control. The study reported presence of defects (kissing-bond, tunneling and joint line remnant) for the triangular, square and hexagonal pins due to inadequate mixing and rotation pulsing [15]. The cylindrical and tapered-cylindrical pins facilitated

better mixing and thus higher joint strengths, with the cylindrical pin providing the best results [15]. For the cylindrical pin, the UTS of the butt joint was measured as 160 MPa [15] and that of the scarf joint as 137 MPa [15], which is a reduction in UTS of about 14%. These results inform that a shallow scarf angle could actually reduce rather than improve joint strength. However, they do not convey any information about how strength varies with scarf angle.

The first study conducted by Sethi et al. [16] in early 2021 also sought to address the potential utility of scarf joints. Their study utilized steep scarf angles with angles of 60° and 75° . They selected 6 mm thick AA6061-T6 plates as their material. The study, similar to Goel et al., used a butt weld as a control. Welds were conducted with a uniform set of process parameters and a tool with a tapered-conical pin. Two welds were conducted for each scarf angle: one in the TAS and one in the TRS configuration, for a total of four scarf welds and one additional butt weld. Sethi et al. also presented a criterion they believe determines the minimum scarf angle tenable without defects, which is given by equation (2.1) [16] and presents minimum scarf angle as a function of pin diameter. As the Sethi et al. [16] study utilized a tapered-cylindrical pin, equation (2.1) includes terms for the root radius (r_{pr}) and tip radius (r_{pt}), with h representing plate thickness. Note that in the case of a straight cylindrical pin ($r_{pr} = r_{pt}$) the fraction collapses to a ratio of pin diameter to plate thickness.

$$\theta_{max} = \arctan \left(\frac{h}{r_{pr} + r_{pt}} \right) \quad (2.1)$$

Of the four scarf configurations tested by Sethi et al., the highest UTS was found for the 60° TAS configuration which had a UTS 13.5% higher than the butt weld [16]. The 75° TAS joint UTS was also larger than the butt weld UTS, the 75° TRS had nearly the same UTS as the butt weld, and the 60° TRS weld had significantly lower UTS than the butt weld [16]. Sethi et al. also observed that the maximum temperatures on the advancing side of the weld were higher for the TAS welds when compared to the TRS welds, and higher for

the 60° TAS weld compared to the 75° TAS weld [16]. Sethi et al. explained this as being due to the tool shoulder area on the advancing side (which has superior heat generation compared to the retreating side) being larger for the TAS configuration compared to TRS configuration. This area is inversely proportional to scarf angle, which seems to align with their temperature results.

The second 2021 study by Sethi et al. [17] is also in relation to scarf joints but is more a study in material processing. It examines the effect of adding different volume fractions (0%, 5%, 10% and 15%) of silicon-carbide reinforcement particles to a scarf joint, with the scarf angle tested being 60° and the configuration being TAS. These joint parameters were likely chosen based on the results of their previous study. The study found that UTS increases with volume fraction in this range as well as hardness, but that ductility appears to decrease [17]. The results of this study display the ability of scarf joints to be used in tandem with material processing techniques to improve strength, but do not have implications for the effect of scarf joint angle on the mechanical or structural properties of welds.

CHAPTER 3

Experiment

3.1 Motivation for Current Study

An independently completed pilot study, within the same time frame as the first Sethi et al. publication, indicated the potential utility of scarf joints. And based off the results of Sethi et al. [16], there seemed a significant amount of room to expand from their results with further investigation.

The first study by Sethi et al. [16] displayed the potential utility of scarf joints for joining AA6061, but also left several unanswered elements which could still be addressed. With only two angles tested it is unclear if their results can be extrapolated to other scarf angles. Although their experiment outlines a potential dependence between scarf angle and joint strength, their study does not utilize enough scarf angles to provide a strong relationship between reported joint properties and scarf angle.

Joint results for lower angles were not investigated, and although they posit the geometric constraint provided by equation (2.1) they do not test its validity. The current study seeks to further examine the relationships between mechanical properties of friction stir welded scarf joints and scarf angle, and potentially address a scarf angle for optimized mechanical properties. The study also seeks to compare results with those achieved by Sethi et al. for 60° and 70° scarf angles, as well as to test the validity of the geometric constraint proposed in equation (2.1).

3.2 Materials

The material selected for this study was aluminum alloy 6061-T6511 plate with a thickness of 0.25-in. This plate was prepared in samples with approximate lengths of 8-in and widths of 2-in. The plate was cut to shape with a combination of a shear press and a vertical band saw to give all weld pieces the desired dimensions.

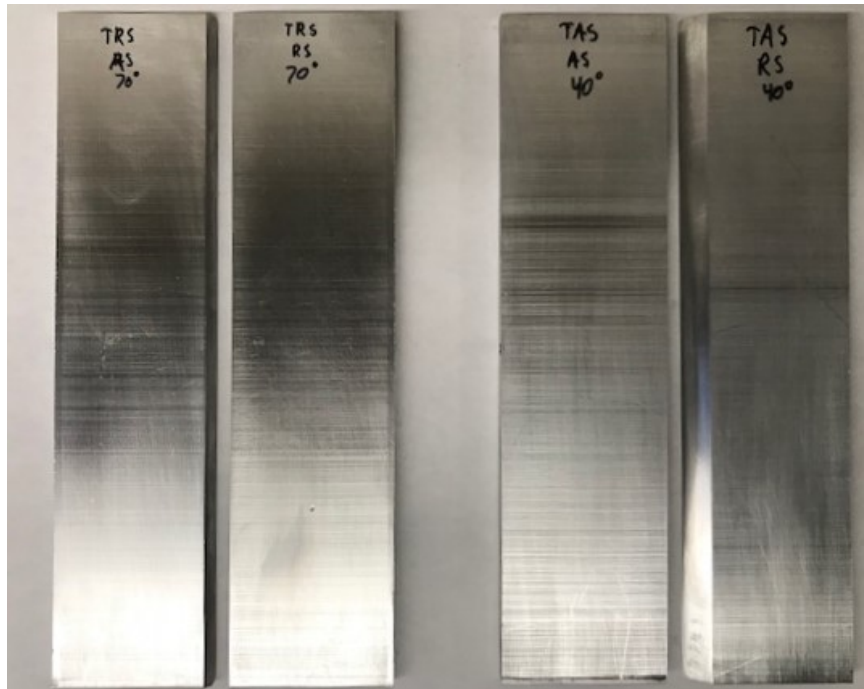


Figure 3.1: TRS 70° and TAS 40° sample pairs as examples of finished weld pieces.

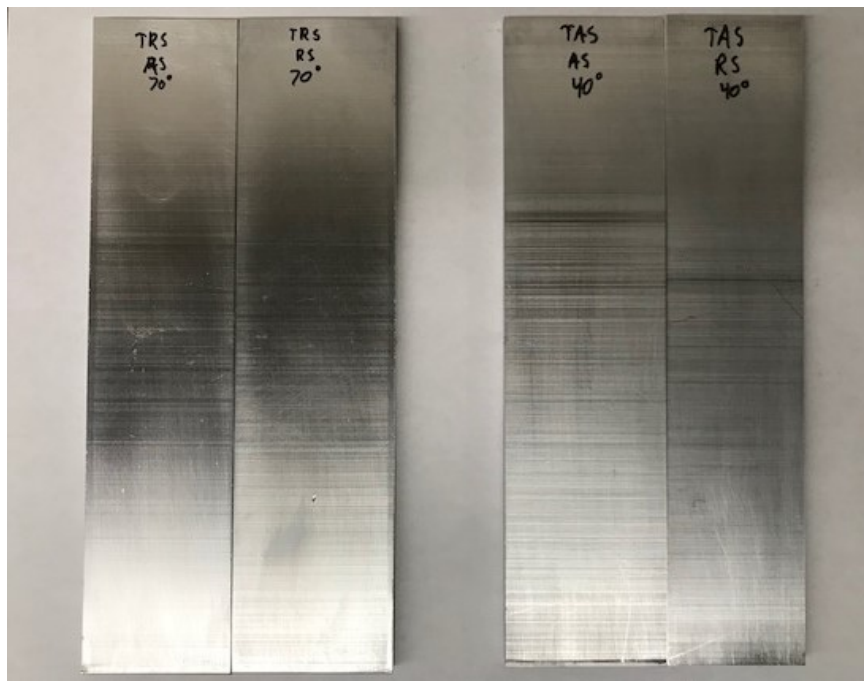


Figure 3.2: TRS 70° and TAS 40° sample pairs, inserted together to display interaction of complimentary faying surfaces.

Each weld piece was faced using a milling machine to ensure accuracy of the critical dimensions, namely the faying and outer surfaces. An angle vice was then utilized with the milling machine for machining the varying scarf angles into the weld pieces. As these surfaces had varying textures, all were sanded to a uniform roughness with 240 grit sandpaper up to 600 grit to ensure that surface roughness was not a factor effecting thermal contact resistance between trials. All weld pieces were surfaced by scouring with steel wool accompanied by polishing with acetone. This was done to remove oxides, oil and other potential inclusions which may have accumulated on the surfaces of the weld pieces. Figure 3.1 and Figure 3.2 display examples of the prepared weld pieces.

3.3 Welding Machine Operation and Force Data Collection

The welding machine utilized for this research was a modified 1944 Milwaukee Model K manual mill, as shown in Figure 3.3. The machine has been retrofitted with electric motors and sensing capabilities to allow for full three-dimensional (x, y and z directions) control of the anvil, and to allow for actuation in these planes to be manipulated contingently. All processes for conducting the welds are automated on the machine, with program directives carried out by custom written programs in a combination of C# and MATLAB/Simulink. This software has been written and added to by multiple graduate students in the Vanderbilt Automation and Welding Laboratory (VUWAL) over the last decade and provides the capability to carry out a wide variety of weld types with variable parameters. Traversal speed, rotation speed, plunge depth, and path type are all controllable via the software. The only process parameter which must be set manually is tool tilt angle. The software also sets process constraints to protect the machine and also acts as an in-process controller via sensor feedback.

The machine is retrofitted with a variety of sensors for localizing and manipulating the apparatus within its operational bounds. This allows for precise weld paths and positional data. It also ensures that the machine will not damage itself by attempting to move be-

yond its range of motion. Optical and linear encoders, as well as string potentiometers, are utilized for these purposes. Additionally, a Kistler 9123C piezoelectric dynamometer mounted above the spindle allows for accurate z-force and spindle torque measurements to be made. These data are very useful for analysis and also protect the machine from applying excessive loads which might damage the machine or its tooling.



Figure 3.3: VUWAL converted Milwaukee Model K manual mill FSW welding machine.

3.4 Weld Parameters and Tooling

The tool used for this study was a 1-inch diameter H13 Tool Steel tool, with a threaded pin having a length of 0.22-in and a diameter of 0.25-in, displayed in Figure 3.4. The convex shoulder of the tool included scrolls to facilitate material transport and heat generation.

This tool design has been found to provide sound weld results for a wide span of process parameters, which was ultimately why it was selected for this study.



Figure 3.4: FSW tool selected for this thesis, featuring a scrolled shoulder and threaded pin. There is some aluminum embedded in the threads and scrolls, but this does not impair function as under operating conditions any material on the tool surface is plasticized.

The welding parameters used in this study were a traversal speed of 3 inches-per-minute (IPM), a rotation speed of 1500 RPM, a tool tilt angle of 1.5° and a plunge depth of 0.215-inches. These parameters were chosen based on the results of a preliminary study, in which these parameters were observed to provide good tool engagement and material mixing, and to produce welds free of voids or other defects. Furthermore, each plunge point was 1-in from the back edge of each weld so that the downward force of the initial plunge would not separate the plates along their butted plane. For the same reason each weld was terminated about 1-in from the front edge, giving each weld a length of ~ 6 -in.

3.5 Temperature Data Collection

A Picolog TC-08 eight channel thermocouple data logger was used as the data acquisition (DAQ) board for this study. Temperature data were collected via two thermocouples. The thermocouples used were two PerfectPrime TL1004 K-Type Thermocouples, selected due to their temperature rating of 500 degrees C. These thermocouples had 0.118-inch diameter steel probes with a length of 1.575-inches. The thermocouples were calibrated using boiling water as a known reference, which confirmed that the thermocouples were operating within the ± 1 degree C specified precision provided by the manufacturer.

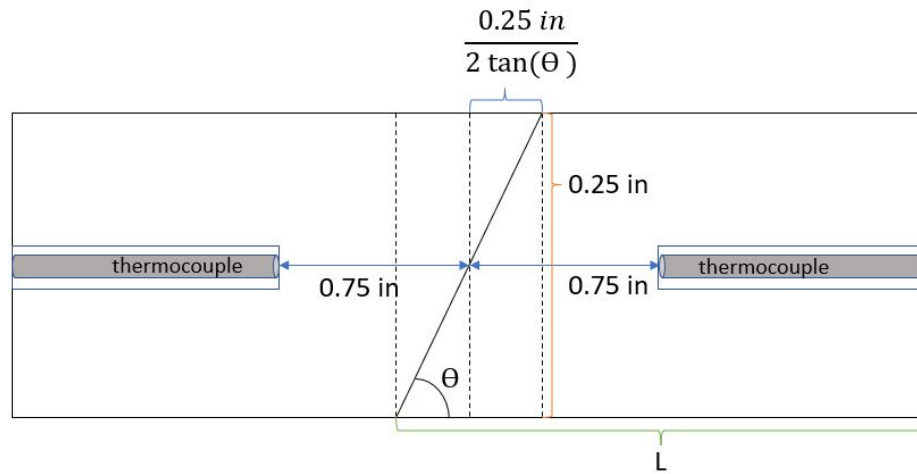


Figure 3.5: Thermocouple mounting and alignment with respect to a cross section perpendicular to the tool traversal direction. Example is provided in the TAS Configuration.

Each weld piece was bored with a 0.120-inch diameter drill bit to allow for insertion of the K-type thermocouples. The bores were made at center length and center width for uniformity across all weld pieces, with the final bore depth calculated to always be 0.75-inches from the central axis of the weld piece regardless of faying surface angle. The thermocouple positioning is displayed in Figure 3.5, along with the geometry used to calculate the bore depth depending on the angle of the scarf joint (depth = $L - \frac{0.25 \text{ in}}{2 \tan(\theta)} - 0.75 \text{ in}$). Figure 3.6 displays the weld apparatus with the thermocouples inserted.

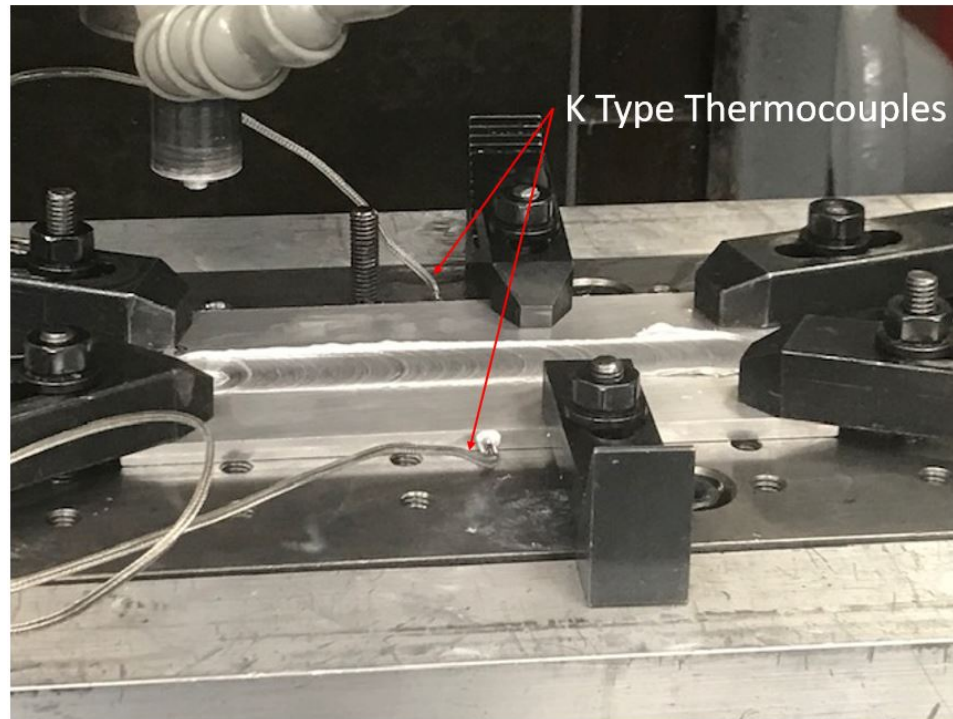


Figure 3.6: Thermocouple positions in weld apparatus.

In addition HY 400 thermal grease was used to improve thermal contact between the thermocouple probes and the weld material. This thermal grease had a thermal conductivity of $1.42 \frac{W}{m K}$, which although low, still gives it 50 times the thermal conductivity of air.

3.6 Final Experimental Setup

The final experimental setup is shown in Figure 3.7. Visible in Figure 3.7 is the Kistler Dynamometer used for measuring spindle torque and z-force, as well as the Picolog DAQ used for collecting temperature data. A vortex tube chiller was used for forced convective cooling of the machine spindle to ensure that the dynamometer was not damaged from overheating. The aluminum test pieces were fixed to the steel anvil of by means of three step clamps per side, which are also visible in Figure 3.7. Hardened spring steel was used as an insert between the weld test pieces and anvil to protect the anvil from process loads. To ensure that the test pieces were square to the anvil the pieces were aligned with a step clamp spaced over two posts before being clamped down. For uniformity, the faying surface of

all welds were approximately centered on the spring steel to mitigate effects of possible height variations on its surface. Welds were conducted in the TAS and TRS configurations for each of the following scarf angles: 80° , 70° , 60° , 50° , 45° and 40° . In addition, a butt weld was also conducted as a point of comparison for the performance of the scarf joints.

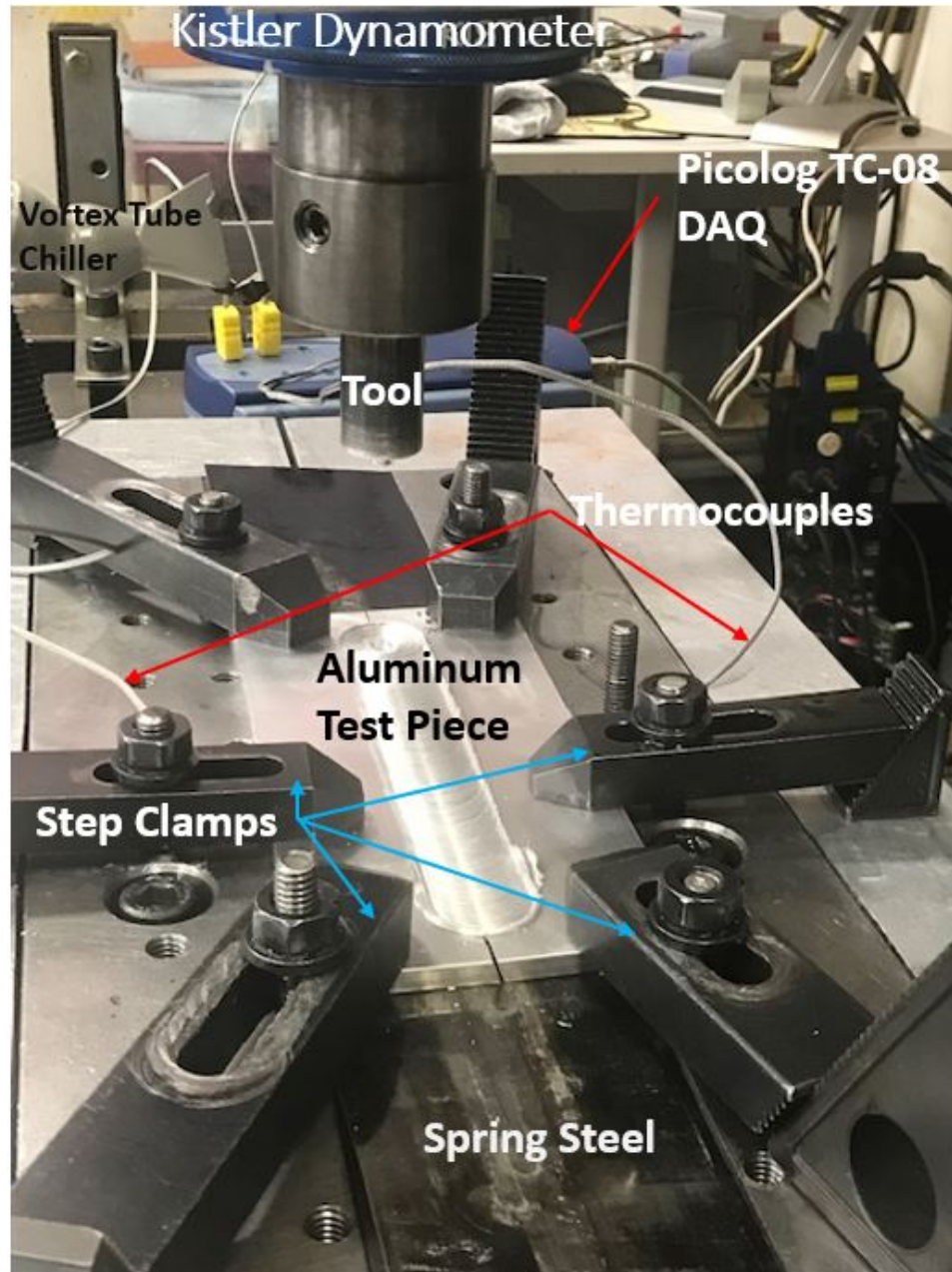


Figure 3.7: Experiment setup for all conducted welds.

CHAPTER 4

Testing and Preparation

4.1 Sample Preparation

For tensile testing, five dog bones were prepared from each of the welds according to ASTM-E8 standards [18]. As such the dog bones had a 1.25-in long and 0.25-in wide test section, with each dog bone clamp section having a width of 0.375-in and a length of 1.25-in. The dog bones had a uniform height of 0.25-in. A manual-mill was used to mill six 0.25-in slots into each weld sample, and a vertical bandsaw was used to cut from the outside edge of the weld samples into these slots to produce the dog bones, as shown in Figure 4.1. This gave the transition from the clamp section to the test section of the dog bones a one-third arc of an 0.25-in diameter circle, per ASTM-E8 standards.

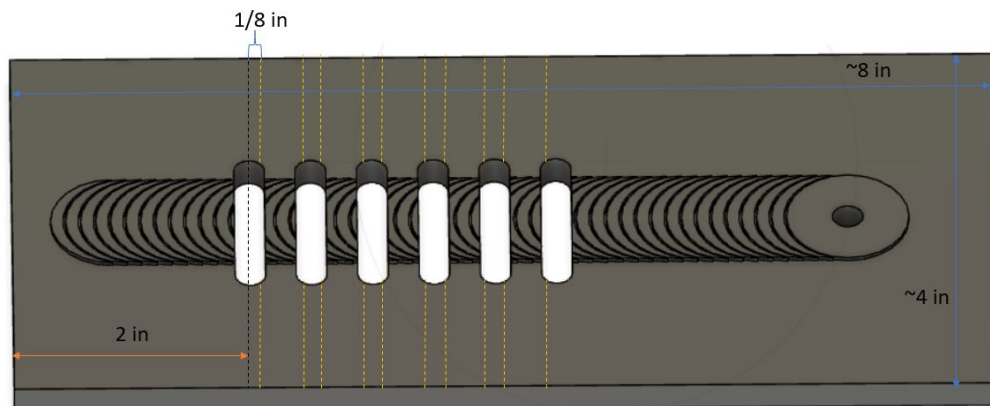


Figure 4.1: Positions from which tensile testing samples were extracted. Dotted lines represent the cuts made to create the dog bones after the weld pieces were slotted with $\frac{1}{4}$ -in slots.

To be representative of the weld as a whole, samples were selected from positions in which the weld process was determined to have been in steady state. There is a transient system response with respect to thermal and structural loads upon the initial plunge of the tool, but as the tool begins traversal these transients subside and yield to steady behavior. As these transients are localized to the area around the tool plunge and initial dwell, the

samples need to be extracted at a distance sufficiently far away from the plunge point, which was determined to be at least 1-in based off the experiment z-force data. However, samples were extracted beginning at 1.125-inches from the initial plunge to provide a small buffer, with the positions displayed in Figure 4.1.

4.2 Tensile Testing

Tensile testing of the weld samples was conducted using a Instru-Met Instron tensile tester, as shown in Figure 4.2. All dog bone samples were filed to remove burs ensuring that there would not be slipping between the tensile tester grips and samples during testing. Additionally, each sample was measured manually with calipers to ensure that accurate cross-sectional area data were recorded for each sample. The AA6061-T6511 plate utilized for the study was nominally 0.25-in thick, however there was some variation in this thickness which necessitated manual measurement of sample thicknesses in addition to sample widths. These measurements are available in Appendix Table A.1. The testing of all samples was conducted with a uniform extension rate of 2-mm/min. The software Test Works was used for control of the Instron tensile tester and data acquisition. Extension, load and time data were collected for each test. The maximum load experienced by each sample (F_{max}) was used in tandem with each sample's cross-sectional area (A_{CS}) to calculate UTS via Equation (4.1).

$$UTS = \frac{F_{max}}{A_{CS}} \quad (4.1)$$



Figure 4.2: Instron tensile tester used for determining sample strength properties.

CHAPTER 5

Results

5.1 Z-Force Results

The forces experienced by the tool can provide insight into process behavior, and one of the strongest indicators is the force applied by the tool on the weld material (which is the z-force). The z-forces for all conducted welds are displayed in Figure 5.1 and Figure 5.2, which show the z-forces measured for the TAS welds and TRS welds, respectively.

Two features present in all of the data plotted in these figures are two spikes in z-force within the first 80 seconds of all welds. The first and smallest of these spikes is caused by the initial plunge of the pin into the work piece. The second, and larger spike, is due to shoulder engagement once a sufficient plunge depth has been reached by the tool. There is a spike in both cases because the material has not been sufficiently heated and so a larger z-force is required to maintain a constant plunge speed. However, once the material is sufficiently heated it can be plastically deformed far more easily, and so does not require as large of a downward force. This is why in both configurations the z-force appears to decrease after reaching a peak. The sharp valley immediately following the second peak denotes the tool dwell period before the tool begins the traversal. But once the traversal has begun and the tool is sufficiently far from the initial plunge position, it achieves relative steady state conditions. Although in broad agreement, there is slight variation among the welds with respect to the temporal dimension for when these features occur. This is mostly caused by lag between weld initiation and plunge start. Another cause is the fact that the pin is not always a uniform height above the work piece, and so there is variation in how far the weld material must be raised to come into contact with the tool.

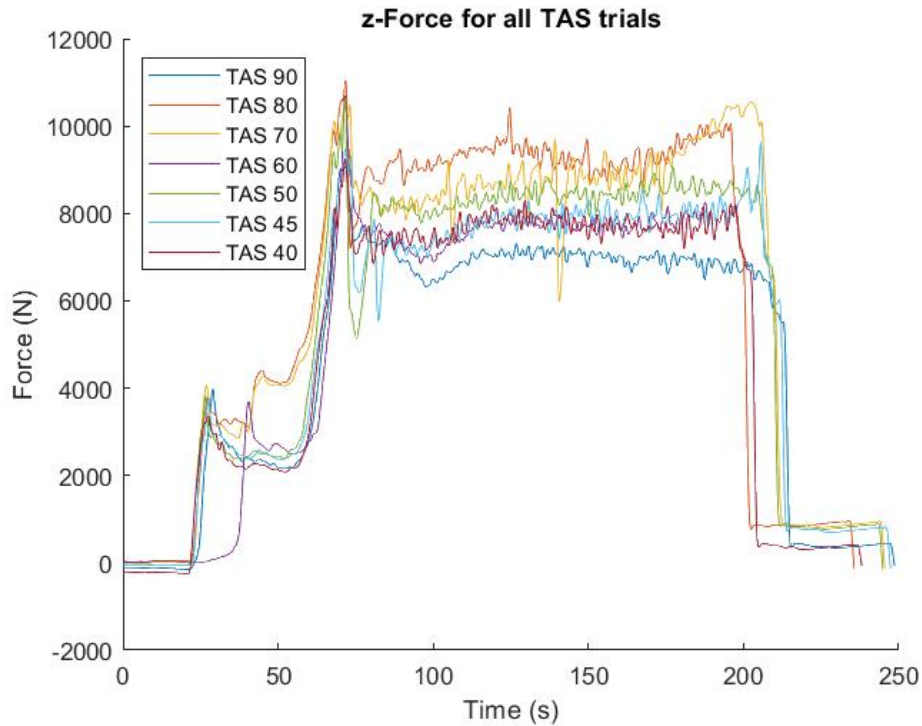


Figure 5.1: TAS configuration: z-forces vs Time for all welds.

In Figure 5.1, z-force appears to vary with scarf angle, and it appears to decrease as scarf angle decreases. This aligns with the results of Sethi et al. [16], who reported a reduction in z-force from their TAS 75° weld to their TAS 60° weld. Figure 5.1 displays larger reductions in z-force between steep angles, like TAS 80° and TAS 70°, but for shallower angles the difference in z-force is far reduced. And for the shallowest TAS scarf angles, 45° and 40°, the difference in z-force is ambiguous. The higher z-force required for large scarf angles indicates that the material is harder to displace, which means that those welds should have less heat generation than lower scarf angles. Based off this it would be expected that steeper scarf joints would experience lower temperatures, and that shallower joints would experience higher temperatures. However, it is also visible in Figure 5.1 that the butt weld has lower required force than all of the TAS configurations. Sethi et al. reported a higher z-force for their butt welds in comparison to their other TAS welds [16]. The lower z-force for this study is likely not indicative of temperature, but rather material transport. Since the

pin is inserted on the weld seam, the tool is more likely to deflect the weld pieces apart, if only slightly. Material extrusion into this gap, however small, would reduce the measured z-force for the weld. For the scarf joints the pin always has a slight offset away from the top of the faying surface, which means that the force of the plunge actually helps to push the plates together rather than apart.

Although the welds should be in a steady state after a sufficient amount of time, these data display a slight increase across all welds. This is likely the effect of thermal expansion of the work piece and anvil causing the shoulder engagement to increase, which would cause a small but gradual increase in z-force. After shoulder engagement, z-force is extremely sensitive to height so that a change in position on the order of a couple thousandths of an inch can measurably increase the z-force. For the TAS 70° weld the large spike at the end is likely a result of the weld piece either lacking uniform thickness or the anvil not providing a uniform height.

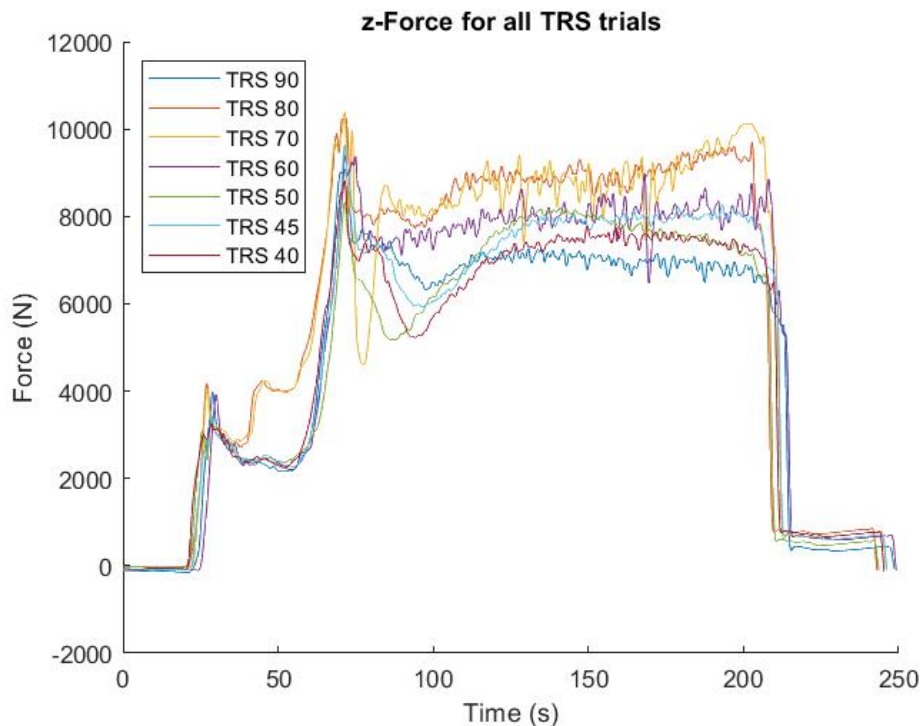


Figure 5.2: TRS configuration: z-forces vs Time for all welds.

The same trends apparent in Figure 5.1 are visible when examining the TRS weld z-force data in Figure 5.2. It appears that for the TRS configuration z-force also decreases with decreasing scarf angle. The TRS 40°, 45° and 50° welds appear to have much larger valleys following the initial shoulder engagement force spike. This could be due to deflection of the weld piece, which is more likely to occur near the start of the weld, but which becomes harder as the tool traverses. Also, the shearing force of the leading edge of the tool is more closely aligned with the scarf seam for the TRS configuration compared to the TAS configuration, which could facilitate slipping between the weld pieces.

In both Figure 5.1 and Figure 5.2 the welds achieve a relative steady state operation by about $t = 120$ s. This steady state value can be approximated by averaging over the interval from $t = 120$ s to $t = 200$ s. These averages are provided for both the TAS and TRS welds in Figure 5.3. The figure clearly shows that z-force decreases with decreasing scarf angle for both the TAS and TRS configurations. However, another interesting result is that the average z-force is, over all, larger for the TAS configurations compared to the TRS configurations. This runs counter to the results of Sethi et al., which showed the z-force to be less for the TAS versus the TRS welds, and that TRS z-force increased from TRS 75° to TRS 60°, the opposite trend to what this study observes.

The reduction in z-force for decreasing scarf angle observed for the TRS welds in this study could be caused by material transport at the leading edge of the tool interacting with the faying surface. The leading edge transports material from the advancing side of the weld towards the retreating side, and at the trailing edge material is deposited from the retreating side towards the advancing side [6]. With the mixing action of the pin the original weld seam is replaced by the material zones discussed in Figure 1.1. However, at the leading edge of the tool the weld seam is still intact below the shear layer in contact with the shoulder. The material transport from the AS towards the RS could cause material induced into motion by the shoulder to be forced upwards by the weld seam, which would cause a slight increase in z-force for the TAS configuration. But material tracing would be

required for verifying if a change in flow pattern is in fact the cause of this result. The main reason for the difference between TRS z-force measurements between Sethi et al. and this study is likely the difference in tool geometry and process parameters, discussed in more detail in Section 6.3.3.

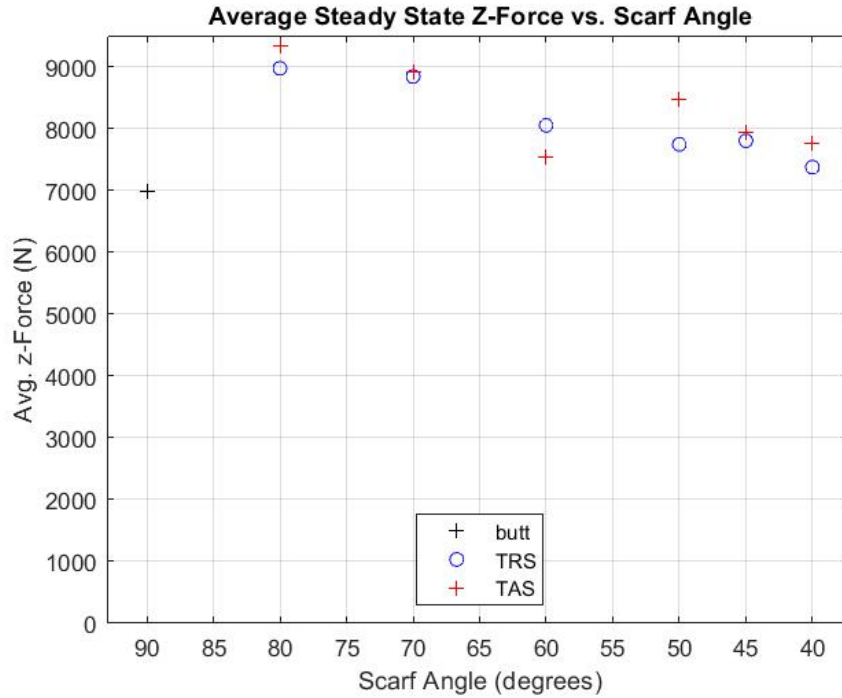


Figure 5.3: Average z-Force for all TAS and TRS welds on the time interval $t = 120$ s to $t = 200$ s plotted versus scarf angle.

5.2 Spindle Torque Results

The spindle torque data recorded from the TAS weld experiments is given in Figure 5.4. Figure 5.5 displays the same for TRS configuration welds. The butt weld spindle torque is included in both figures as a reference. Common features of both figures are initial readings near zero, which are due to data recording before the spindle motor has actually activated. Upon startup, the spindle reads a negative torque as there is very little resistance to rotation and so the controller must reduce torque to maintain the desired rotation speed. Upon the initial plunge of the pin the torque increases, and it appears to increase almost linearly until it reaches its maximum, which corresponds to full shoulder engagement and the start of tool

traversal. Over the total run time of the weld torque appears to decrease in both figures, which is due to increased heating of the material causing it to plasticize more easily.

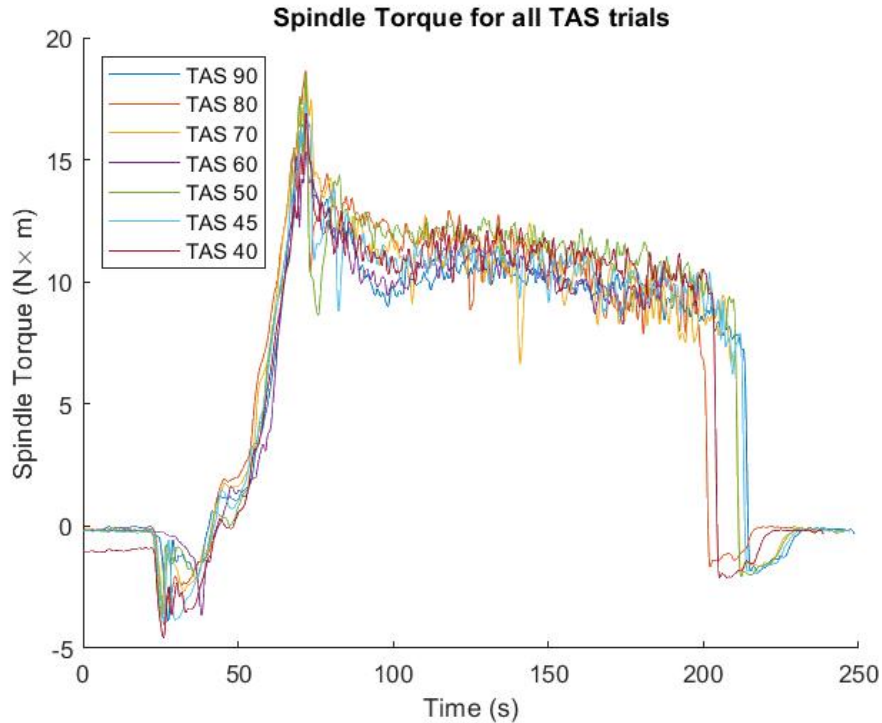


Figure 5.4: TAS configuration: Spindle Torque vs Time.

Spindle torque, like z-force, is accepted to be an indicator of the material temperature [19]. A reduction in spindle torque between trials should indicate a comparatively higher temperature for the welded material. Figure 5.4 and Figure 5.5 exhibit similar behavior to the corresponding z-force data with respect to peaks due to initial plunge, followed by steady behavior. However, unlike the z-force data, there is very little variation between the welds, and although it would be expected that torque would decrease with a decrease in scarf angle based on the z-force results, this behavior is not observed.

The average torque over the steady state portion of these welds (approximately $t = 125s$ to $t = 200s$) is provided in Figure 5.6. These averages display how little variation there is between the welds, and indicate that there is not a strong relationship between spindle torque and scarf angle. Whether the weld is in the TAS or TRS configuration also does not appear to have a clear effect on spindle torque. This seems to indicate that dependence

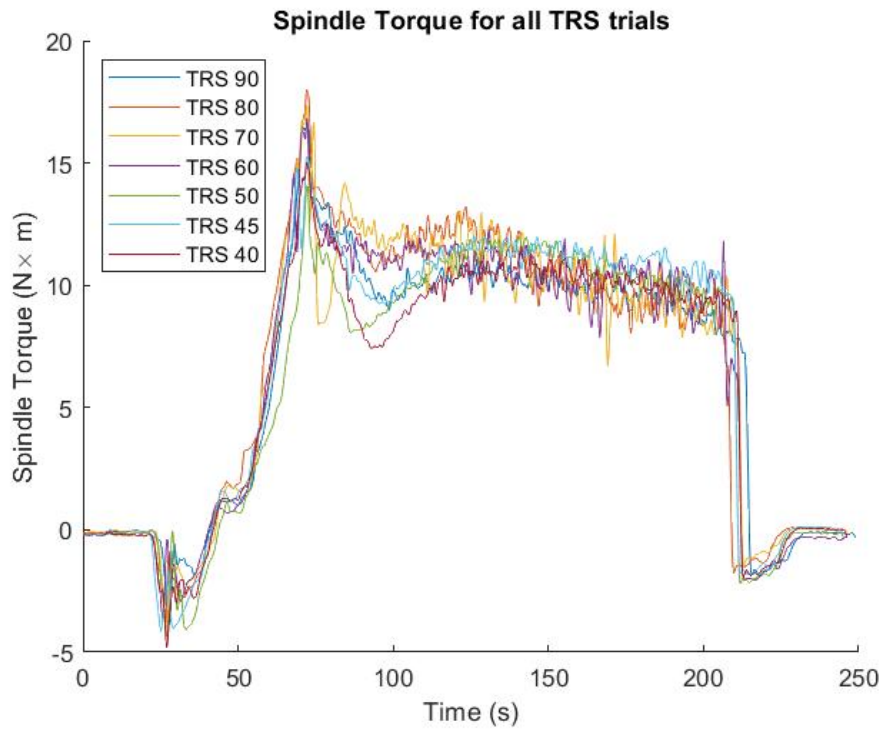


Figure 5.5: TRS configuration: Spindle Torque vs Time.

of required spindle torque on temperature is weaker than is the case for z-force, so that although in actuality a dependence may be present, it is not distinguishable. The somewhat lower steady torque exhibited by the butt weld is likely due to deflection of the plates due to the pin, with the small gap created allowing for material extrusion to relieve forging pressure, which would also decrease required torque.

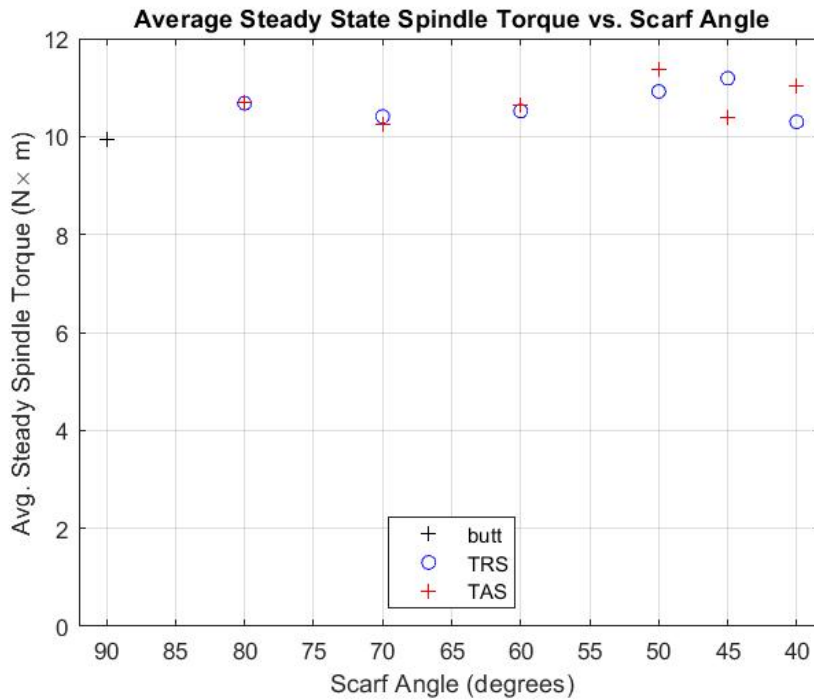


Figure 5.6: Average Spindle Torque vs Scarf Angle for all welds.

5.3 Temperature Results

As discussed previously, the tool shoulder is most responsible for heat generation in the FSW process. For a butt joint with a centered pin the shoulder area is equal on both weld pieces, but for the scarf joints it is a function of scarf angle.

Whether in the TAS or TRS configuration, the top scarf plate will see a larger shoulder contact area, and the bottom plate will see a smaller shoulder contact area. This informs that the top plate temperature should always be larger than the bottom plate. Additionally, as scarf angle decreases the top scarf plate experiences an increase in shoulder area contact, while the bottom scarf plate experiences a decrease in shoulder area contact. This relationship is displayed in Figure 5.7. Due to this relationship, as scarf angle decreases the TAS configuration should show an increase in the AS temperature and a decrease in RS temperature. Conversely, the TRS configuration should see an increase in RS temperature and a decrease in AS temperature.

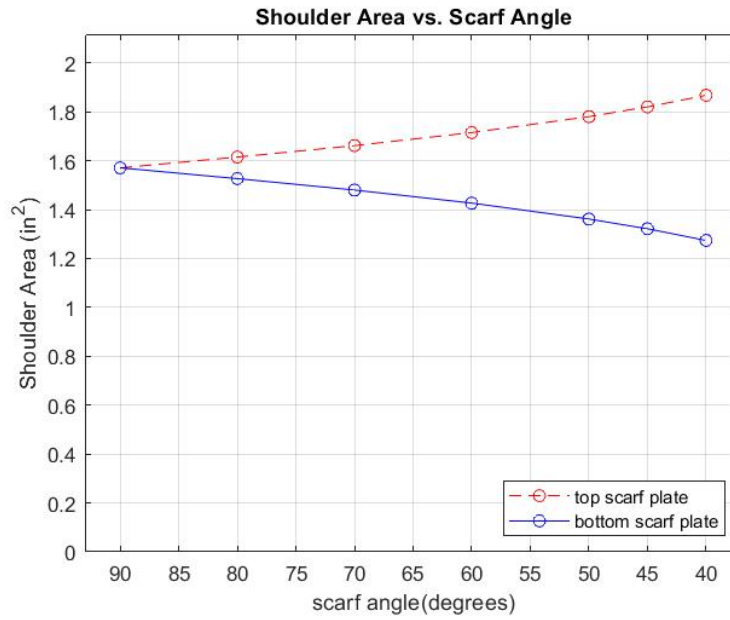


Figure 5.7: Shoulder contact area as a function of scarf angle, displayed for both the bottom and top scarf plates.

The individual temperature results for all welds are displayed in Figures 5.8-5.11. For all TAS welds, the AS temperature is larger than the RS temperature, and for the TRS welds the RS temperature is larger than the AS temperature. These results perfectly align with the expected behavior, and corroborate the results obtained by Sethi et al. [16].

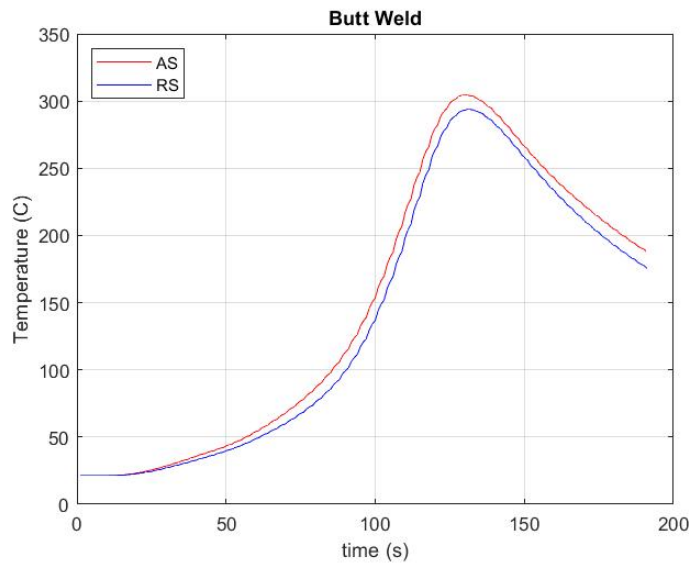


Figure 5.8: Butt weld temperature results

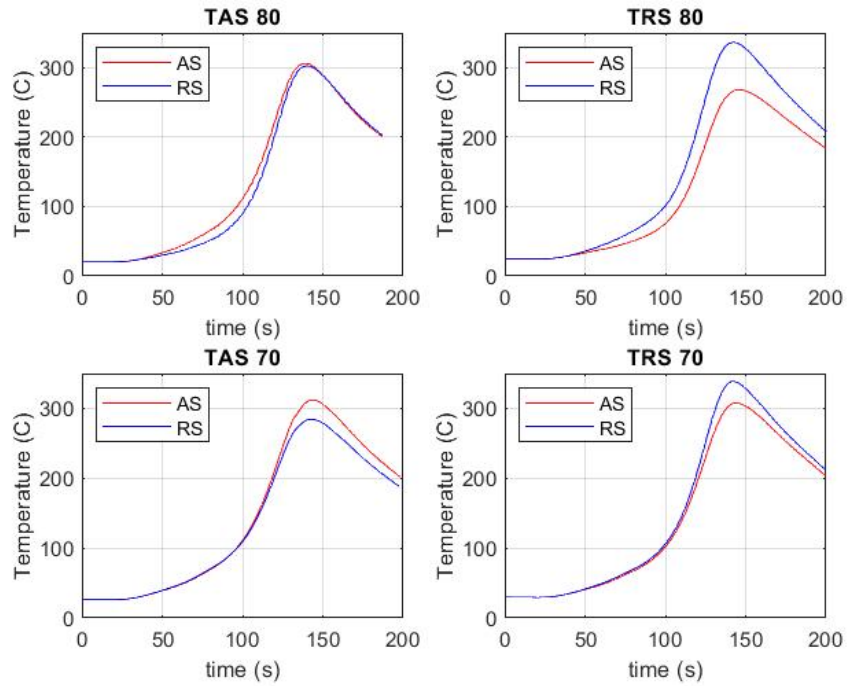


Figure 5.9: 70° and 80° scarf weld temperature results.

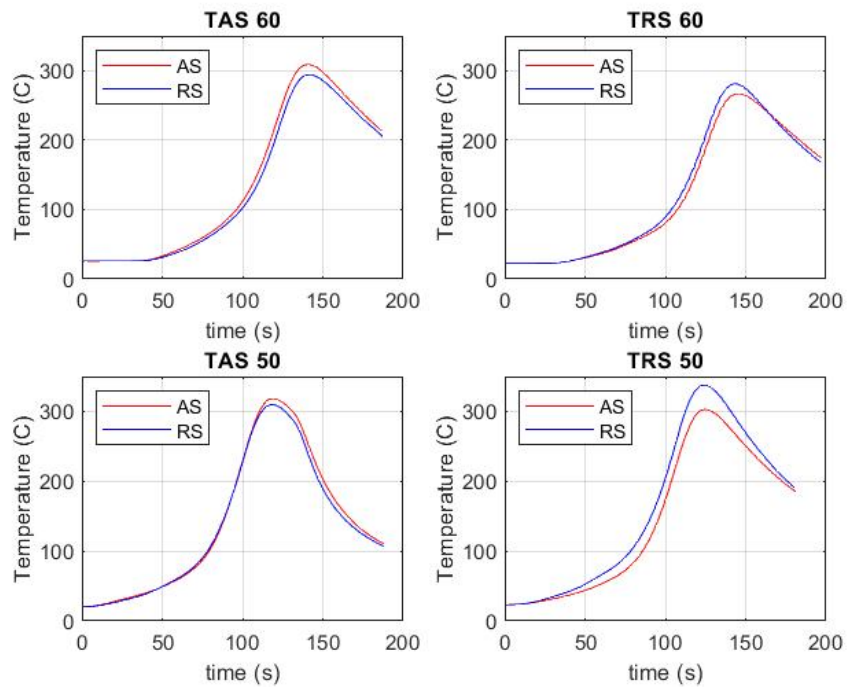


Figure 5.10: 50° and 60° scarf weld temperature results.

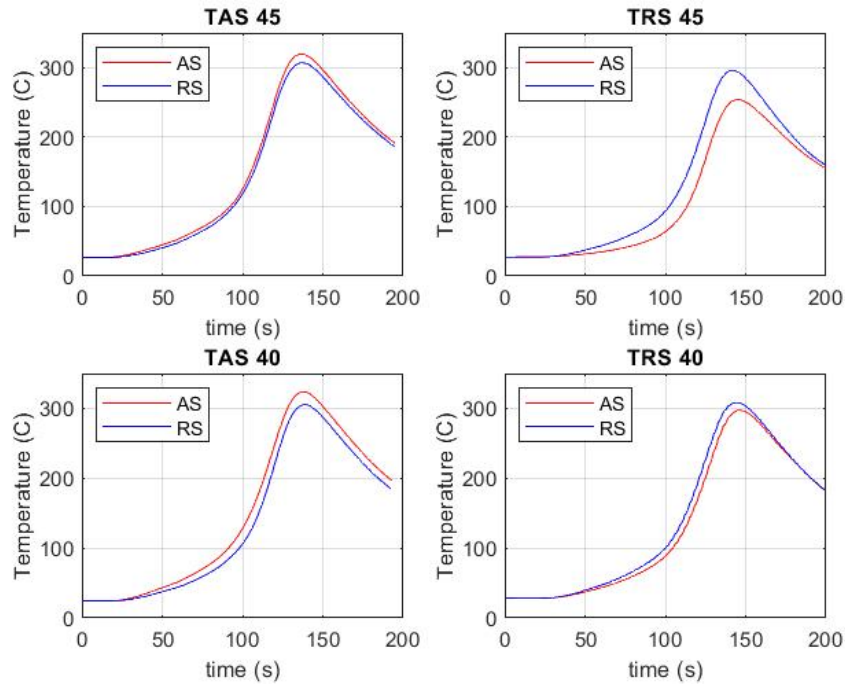


Figure 5.11: 40° and 45° scarf weld temperature results.

These temperature data were recorded from the initial tool plunge until tool extraction, but there was some variation in capture length, as is visible in these figures. This variation does not affect the data fidelity, but accounts for a positive or negative shift with respect to time. As the data of interest were the magnitude of temperatures reached when the tool was even with the thermocouples, the timing of the captures has no bearing on the results.

All thermocouples were positioned a uniform distance of 0.75-inches from the center of all weld seams (0.25-in from the shoulder), so that peak temperatures across all welds provided a reasonable point of comparison. Figure 5.12 displays the maximum temperatures recorded for both the AS and RS across all TAS welds. From this figure it is visible that there is not a large variation in temperatures among the conducted TAS welds. The AS results align with the expectation of AS temperature increasing with decreasing scarf angle; with the maximum AS temperature of 324 degrees C recorded for the TAS 45° scarf joint, and the minimum AS temperature of 304 degrees C recorded for the butt joint (90° scarf joint). These results also align with those indicated by the decrease in z-force demonstrated

in the previous section. However, there is only a temperature difference of 20 degrees C between these extremes. RS maximum temperature was expected to uniformly decrease with decreasing scarf angle, but the data do not display this relationship. A minimum of 284 degrees C was achieved for the TAS 70° joint, and a maximum temperature of 310 for the TAS 50° joint. These data do not appear to support a dependence of maximum RS temperature on scarf angle, as there is too much variation to display any meaningful trends.

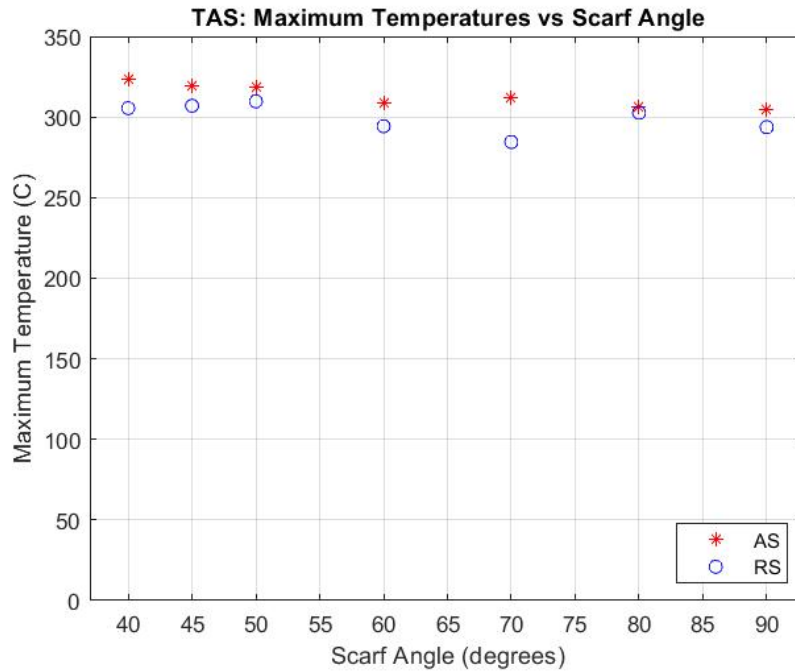


Figure 5.12: Maximum AS and RS temperatures for all TAS welds vs Scarf Angle.

Figure 5.13 displays the maximum AS and RS temperatures recorded across all TRS welds. These data also do not appear to display a clear dependence between maximum temperature and scarf angle. The expected behavior was that maximum RS temperature would increase with decreasing scarf angle, and that AS temperature would decrease; an effect related to the changes in shoulder contact area discussed previously. However, these expected behaviors are not visible in these results. The data do confirm the expected behavior of RS temperature being greater than AS temperature for all TRS welds, but do not support the other expected trends.

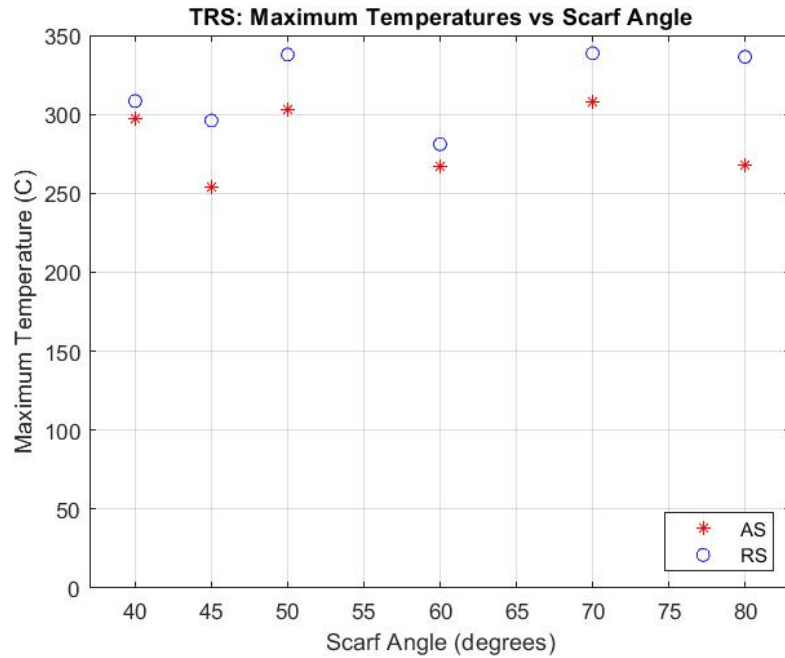


Figure 5.13: Maximum AS and RS Temperatures for all TRS welds vs. Scarf Angle.

The apparent lack of dependence between maximum temperature and scarf angle for the TRS welds could have several causes. The thermocouples were only 0.25-in from the weld center, and so small variations in thermocouple depth could disproportionately impact temperature readings. For the same reason pin alignment bias towards either the AS or RS would induce a similar error in the measured temperature data, while z-force, spindle torque and mechanical properties would not be significantly affected. The short distance from the weld center was meant to more accurately capture the magnitude of temperatures reached in the weld region, but these data indicate that a further distance is beneficial as it can better attenuate error, even if the temperatures measured are of a lower magnitude.

5.4 Tensile Testing Results

The load applied over the duration of the test was recorded for each tensile test of the weld samples. The maximum load experienced by each sample was divided by the cross-sectional area of each sample (provided in the Appendix as Table A.1) to determine its UTS. The UTS of the five samples taken from each weld were then used to determine an

average UTS for that scarf angle and configuration (either TAS or TRS). These results are represented in Figure 5.14, with the exact values provided in Table 5.1.

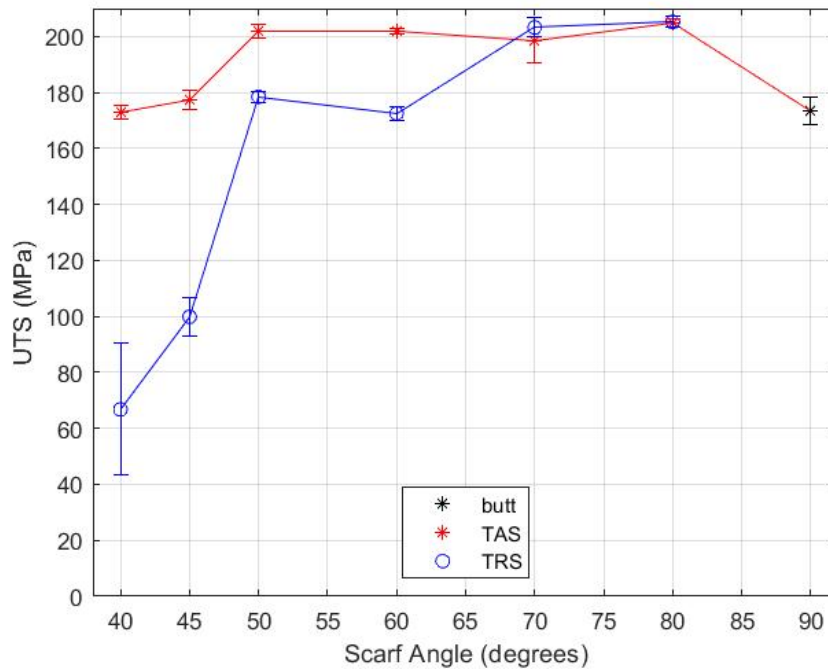


Figure 5.14: Average UTS of all TAS and TRS welds plotted versus scarf angle. Error bars represent the standard deviation of each weld's five tensile samples.

5.4.1 Large (60° to 80°) Scarf Angle Results and Discussion

In Figure 5.14 it is clear that the UTS of the TAS scarf welds with angles between 80° and 45° exhibit better tensile strengths than the butt configuration. However, it is also visible in Figure 5.14 that the UTS initially increases for the TRS welds with 80° and 70° scarf angles. The UTS of these welds do not hold a statistically significant difference with their counterpart TAS welds, and given the small difference in shoulder and pin contact area on the AS between the TAS and TRS configurations for these angles, it is reasonable that these welds would not exhibit a significant difference in UTS. The TRS 80° weld does hold the largest average UTS of all trials with a UTS of 205.2 MPa, which is counter to the expectation that a TAS weld should have the largest UTS. But considering the standard deviations of the TAS and TRS 70° and 80° scarf joints, this result is likely not indicative

of an optimization. These data seem to indicate that there is not significant difference between the TRS and TAS configurations for these angles, and support the fact that these configurations outperform the square butt configuration. The reduced strength of the butt configuration compared to the scarf welds aligns with the reduction in z-force compared to most scarf welds discussed in a previous section, and so is expected.

Angle	Configuration	Avg. UTS (Mpa)	Std. Dev.(Mpa)	Coeff. Variation (%)
90	Butt	173.4	5.1	2.9
80	TAS	204.8	1.3	0.6
80	TRS	205.2	1.9	0.9
70	TAS	198.7	8	4.0
70	TRS	203.3	3.4	1.7
60	TAS	202.0	1.1	0.5
60	TRS	172.5	2.5	1.4
50	TAS	201.7	2.4	1.2
50	TRS	178.5	1.8	1.0
45	TAS	177.5	3.4	1.9
45	TRS	99.9	6.8	6.8
40	TAS	172.9	2.54	1.5
40	TRS	66.8	23.6	35.4

Table 5.1: Average UTS, standard deviation, and coefficient of variation of all TAS and TRS scarf welds.

Examining the other TAS welds, the UTS of the welds from 80° to 50° only reduces by 3.1 MPa, which is only 1.5% of the TAS 80° weld's UTS value. This is comparable to the coefficients of variance for most of the TAS welds, which indicates that for these steep to medium scarf angles the UTS is not significantly affected by scarf angle. However, the 80° scarf angle does provide the greatest UTS of all TAS welds at 204.8 MPa. Although the average UTS for the TAS 70° weld is the lowest of these four welds, it also has the largest coefficient of variation at 4%, which makes it ambiguous whether this result is meaningful. The coefficient of variance for the TAS 80° , 60° and 50° welds is exceptionally small (0.6%, 0.5% and 1.2% respectively), which indicates that these welds are good quality and defect-free. The same is true of the TRS welds from 80° to 50° (coefficients of variation

visible in Table 5.1). The only outlier is the TAS 70° weld with a coefficient of variation at 4%, which is likely due to variations in plate thickness marginally affecting shoulder engagement and material extrusion.

The results seem to support a large operating window of high strength welds in the TAS configuration from TAS 80° to TAS 50°. They also indicate the possibility of an optimum scarf angle between 80° and 70°, but given the standard deviations of the data this result is not strongly supported. The data furthermore demonstrate that for steep scarf angles there is not significant difference between the TAS and TRS configurations, but that this factor is significant for scarf angles less than ~70°.

5.4.2 Small (40° to 50°) Scarf Angle Results and Discussion

Sethi et al. [16] did not include scarf angles smaller than 60° in their study, so the results of the 50°, 45° and 40° scarf welds give novel insight into weld behavior for these smaller scarf angles. Although there was virtually no difference between the TRS and TAS welds with 70° and 80° degree scarf angles, there is a clear reduction in UTS for the TRS welds compared to the TAS welds from 60° downwards. And this difference in UTS seems to generally increase as scarf angle decreases. Although TAS welds also see a UTS reduction following 50°, the reduction in the UTS of TRS welds is drastic. The percent reduction in UTS from the TAS 50° to the TAS 40° weld is 14.3%, while the percent reduction in UTS from the TRS 50° to the TRS 40° weld is 62.6%.

Utilizing the equation for scarf angle limit proposed by Sethi et al. [16] in equation (2.1), with a pin diameter $d = 0.25$ -in and a plate thickness $h = 0.25$ -in, the maximum angle tenable for defect free joints would be 45°. Given the standard deviation in plate thickness across all welds was 0.007-in, this theoretical maximum should lie within the bounds of 45.8° and 44.2°. Figure 5.1 shows that there is a significant reduction in UTS for both TAS and TRS welds following 50°. However, the precision of the TAS 45° and 40° welds' data indicate that although these joints are mechanically weaker than larger angles,

they are still free of major defects. A main reason why they exhibit lower UTS could be the larger heat input experienced, which would cause the HAZ to see increased grain growth, which in turn could cause a reduction in overall tensile strength. The precipitous drop in UTS and increase in variation for the TRS welds at these angles displays that the scarf angle limit in equation (2.1) does apply reasonably to the TRS configuration. These TRS results are likely due to reduced heat input towards the weld root reducing material mixing and extrusion, which could cause defects. Overall, these results indicate that equation (2.1) does provide a reasonable criteria for estimating where UTS can be expected to decrease for the TAS welds, but does not predict the cut-off for weld defects as intended for TAS welds. It does fulfill this function for the TRS welds however.

5.4.3 Comparison With Study by Sethi et al.

The current study's results for the 80°, 70° and 60° scarf welds stand in contrast to those obtained by Sethi et al. [16], which reported a clear increase in UTS from TAS 75° (245 MPa) to 60° (~267 MPa), and reported UTS for the TRS 75° weld as ~158 MPa and the TSR 70° weld as ~210 MPa. They also reported the highest UTS for the TAS 60° weld, which had a 13.5% difference with the butt configuration (~228 MPa). The differences between the results of this study and those of Sethi et al. are likely due to the selection of process parameters and tooling, as well as the dimensions and geometry of the pin. These are provided categorically in Table 5.2.

Overall, the slower rotation, faster tool traversal, and smaller shoulder diameter of the Sethi et al. study means that their tool should have had reduced heat input compared to that of the current study. This could allow for the variation in heat production between the TAS and TRS configurations to be more detectable at steeper scarf angles, whereas the higher rotation, larger diameter shoulder, and slower tool traversal of this study could mean that the material is more thermally saturated, so that small changes in shoulder contact area do not impact results as significantly.

Study	Rotation (RPM)	Traversal (IPM)	Plunge (in)	Tool Tilt	Plate Thickness
Sethi et al.	1100	4.72	X	2°	0.236
Current Study	1500	3	0.215	1.5°	0.25
	Weld Length (in)	pin d_{root} (in)	pin d_{tip} (in)	pin length(in)	$d_{shoulder}(in)$
Sethi et al.	4.72	0.236	0.157	0.228	0.71
Current Study	6	0.25	0.25	0.22	1

Table 5.2: Tool geometry and process parameters used by Sethi et al. and current study. Appropriate values converted to imperial units for direct comparison.

The difference in tool tilt angle between the studies could also be a potential factor, but tool tilt is not a significant contributor to temperature or weld strength results [11]. But regardless, the tooling and process differences could have a large impact on where, if any, an optimization for UTS would occur as a function of scarf angle. Given the precision of the UTS data gathered in both studies, this strongly supports that process parameters are non-negligible factors affecting the strength of scarf joints, and that tool and pin geometry specifically appear to have sizable impacts on results.

5.5 Fractography Analysis

Examining a macroscopic view of the joint failures for each of the thirteen welds lends useful insight into joint behavior. Figure 5.15 displays one tensile test sample from each of the tested welds. The samples were selected to be representative of joint failure for each weld as a whole, although there was some variation in failure mode among the five dog bones for some of the welds.

Examining the failure sites of the presented samples, it is visible that there is some common behavior related to scarf angle. Since the AS of the weld generally experiences higher temperatures than the RS, the HAZ on the AS is expected to see more grain growth due to recovery. And as the HAZ closest to the TMAZ experiences the highest temperatures without the benefit of plastic deformation to induce dynamic recrystallization, the HAZ/TMAZ interface on the AS is a common failure point. This can be explained by the Hall-Petch

relationship, which is an empirical relation between hardness and grain size provided in equation (5.1), where H_0 is base hardness, d is grain diameter, and k_H is a constant for that material [20].

$$H = H_0 + k_H \sqrt{d} \quad (5.1)$$

As hardness relates to strength, this indicates that an increase in grain size reduces strength, while a decrease in grain size increases strength. Ductility is also indicative of larger grains, while small grains cause material to be more brittle [20]. The HAZ on the RS also sees a similar effect, and for this reason defect-free-joint failures typically occur in these portions of the weld. With respect to modes of failure, a ductile failure mode is characterized by dimples and necking of the material [21], whereas a brittle mode will show sharp planar facets [20]. Joint failure is often a mixed mode with characteristics of both failure types, and FSW joints typically display ductile failure. But the extent to which these modes are present in the failure communicates useful information about the properties of the joint.

For the larger scarf angle welds in Figure 5.15, the butt joint, TAS 80° , TRS 80° , TAS 70° , TAS 60° and TRS 60° welds all display failure towards the AS, which aligns with expectation as discussed. The TRS 70° weld does display a fracture towards the RS, but this is not anomalous as there are other factors in play which can dictate failure location, including test-piece cross-section and dispersal of alloying elements in the metal matrix. There is often not a large difference between HAZ material properties between the AS and RS, and so failure can occur in either depending on the presence of additional factors. On the micro-scale the material is not homogeneous in composition, which can also cause variations in behavior. But the macro-scale observations on fracture modes can still be used reasonably to characterize joint behavior.

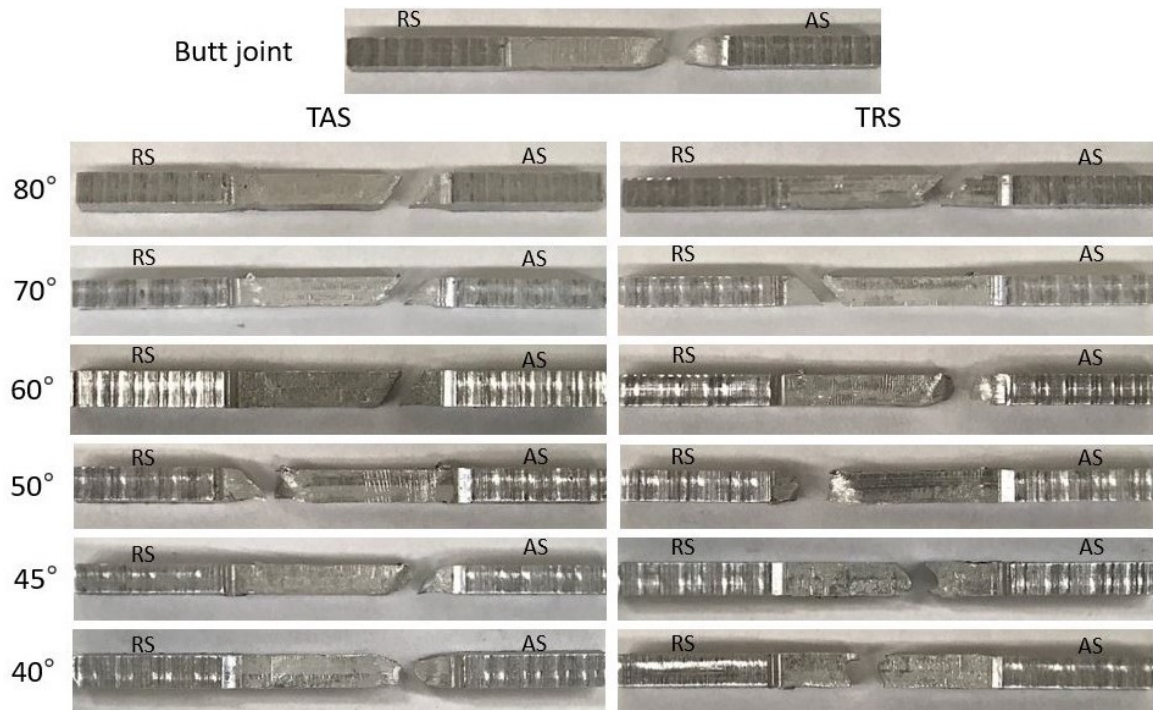


Figure 5.15: Examples of fractures observed for each of the conducted welds. Samples were selected to best reflect the fracture modes of their respective weld sets.

The butt joint displays some necking which indicates a more ductile mode of failure compared to the other steep-angle joints, but TAS 80°- 60° and TRS 80° and 70° welds all display well-defined fracture interfaces, which is indicative of a comparatively more brittle mode of failure. The slope these fracture surfaces display is due to the decrease in size of both the TMAZ and HAZ when traveling towards the bottom of the weld piece as shown in Figure 1.1. This causes the TMAZ and HAZ interface to be on a slope, which is why a slope is displayed in the failure surface. The reduction in necking and interface deformation of these failures is an indicator of material hardness, which in turn informs that these joints likely have more refined grains compared to other welds. This aligns with the z-force results for these welds. Increased z-force should indicate reduced temperature compared to other welds. This implies a reduction in HAZ grain growth and increased strength.

The TRS 60°, TAS 50° and TRS 50° welds all display slightly more necking, and other ductile failure indicators such as dimpling, in comparison to previous welds. This indicates that these welds should have slightly larger grain sizes, and so slightly reduced strengths. This is corroborated by the UTS results in the previous sections.

The fracture interfaces of the 45° and 40° scarf welds displayed the greatest deviation in comparison to the other welds, and so close-up images of the fracture surfaces were taken to investigate failure behavior, which are shown in Figure 5.16. The AS is displayed above the RS in both cases, and each pair is aligned so that the top of each weld is on the left-hand side and the bottom of each weld is on the right-hand side (indicated by the root). For the TAS welds at these angles in Figure 5.15 it is visible that the 40° joint displays far more necking compared to the 45° joint. This aligns with the result of reduced UTS from TAS 45° to TAS 40° observed in the previous section. The fracture of the TRS 45° and 40° samples explains the abysmally low UTS observed for both joints in the previous section. Both exhibit brittle failure in portions of the weld seam in Figure 5.16.

It appears that crack propagation begins at the root, and follows the onion ring grains of the weld structure up through the weld. In both cases the crack propagates around the nugget as it can more easily propagate through the increased grain boundaries in the TMAZ. And in both cases there is a visible cessation the crack as it reaches the top of the weld. This is due to the top layer exhibiting different material properties due to extreme plastic deformation from the shoulder, which facilitates dynamic re-crystallization inducing better strength and reduced ductility. This causes the initial crack to cease upon reaching this layer. The final failure of the joint is completed by ductile failure of this layer as the axial load persists. This sequence is also visible in the raw tensile data for these welds provided in the Appendix as Figure A.3 and Figure A.1. The cause of the initial crack propagation is likely a kissing bond or root defect at the weld root, which could be due to reduced heating of the TRS RS preventing material from being adequately plasticized for proper bonding of the material at the base of the scarf joint.

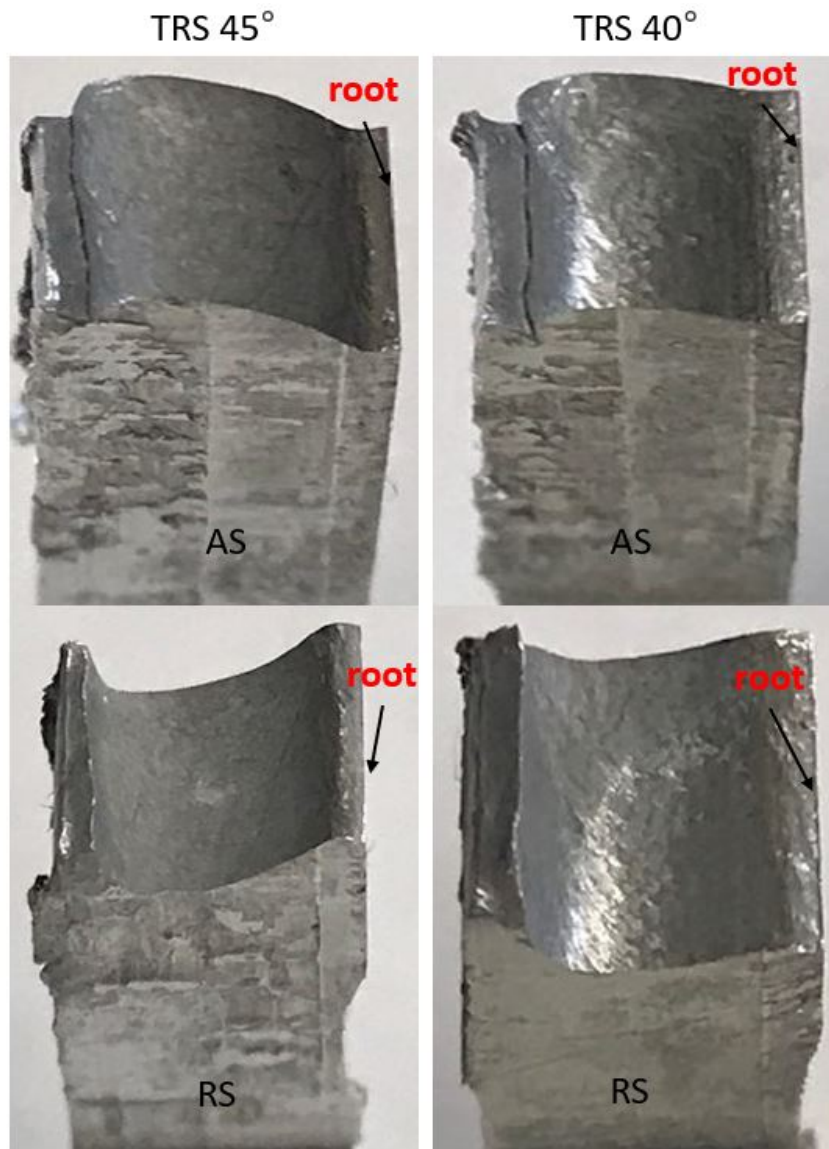


Figure 5.16: Close up imaging of the TRS 45° and TRS 40° joint failures.

CHAPTER 6

Conclusions

This study examined the properties of welds conducted with FSW on variable scarf joint geometries. Two different scarf joint configurations (TAS and TRS) were paired with six different scarf angles between 40° and 80° to produce twelve scarf joint welds, and one additional butt joint weld for comparison. Temperature, z-force, spindle torque, and ultimate tensile strength (UTS) were collected in order to parameterize the results. From these collected data several conclusions about the welding of scarf joints can be drawn.

Although temperature data did not strongly support relationships with scarf angle, they do provide conclusive proof that the greater shoulder contact area for the top plate in the scarf joint leads to that side of the weld reaching a higher temperature, independent of configuration. All TAS welds reported a larger AS temperature compared to the RS, and all TRS welds reported a larger RS temperature compared to the AS.

The z-force data displayed a positive relationship with scarf angle for both the TAS and TRS configurations: as scarf angle decreases z-force also decreases. The reduction in z-force for TAS welds as a function of scarf angle aligned with results of Sethi et al. which also displayed decreasing z-forces. But for the TRS welds the results of the current study conflicted with those of Sethi et al, as they reported an increase in z-force for TRS compared to TAS; whereas this study observed a z-force decrease with decreasing scarf angle for both configurations. This difference is believed to be due in large part to the selection of different process parameters and tooling between these studies. Spindle torque data were inconclusive and displayed very little variation between the welds conducted in the study, in contrast to the z-force results.

The tensile testing of the specimens revealed the most interesting results. A maximum UTS of 205.2 MPa was achieved by the TRS 80° configuration, with the second highest of

all welds being the TAS 80° weld's UTS of 204.8 MPa. But given standard deviations of 1.9 MPa and 1.3 MPa respectively these results do not support that the TRS 80° is actually stronger than the TAS 80°. The extremely similar UTS of the TRS and TAS 70° welds coupled with the TAS and TRS 80° welds' results shows that for steep scarf angles there is not a significant difference between the TAS and TRS configurations. The TAS and TRS 80° welds displayed an 18.1% and 18.3% increase in UTS when compared to the butt weld (173.4 MPa).

The TAS welds (70°, 60°, 50° and 45°) showed 14.6%, 16.5%, 16.3% and 2.4% increases in UTS in comparison to the butt weld. The decrease in UTS for the TAS welds from 50° to 45°, and 45° to 40° shows that best results are achieved between TAS 80° and TAS 50° for the chosen weld parameters. The difference in UTS between the TAS 80° and TAS 50° welds of only 3.1 MPa displays that there is a wide range of scarf angles available for producing high strength welds in the TAS configuration, which is a promising characteristic of scarf joints in the context of manufacturing. But the data do not strongly support a scarf angle for optimized UTS due to the low variation in UTS within the same range. However, based on the results it does appear that a joint optimization could be achieved with a scarf angle close to 80°.

The TRS configuration experiences a marked drop in UTS in comparison to TAS welds of the same angle at lower scarf angles. The TRS 40° displayed only 38.5% of the butt joint's UTS, whereas the TAS 40° weld displayed 99.7%. This indicates that the TAS configuration is superior to the TRS configuration (despite close alignment for steep angles) due to a wider range of tenable scarf angles for joining. This is likely due to a combination of reduced heating and mixing of the weld material, a result influenced by the pin diameter and tool tilt but also the scarf angle, which would control this mechanism in the face of constant process parameters.

These results also revealed that the geometric criteria for joint stability provided by Sethi et al. must be applied separately to the TRS and TAS configurations, as sound TAS

welds were fabricated below the expected maximum angle of 45° predicted by equation (2.1).

This thesis overall demonstrates that scarf joints can represent an improvement over butt joints. The TAS scarf configuration has been demonstrated superior to the TRS scarf configuration due to a larger range of tenable scarf angles; and the wide range of effective scarf angles for TAS also demonstrates process robustness. All of this indicates the potential for this joint configuration and the possible utility for adoption in manufacturing processes.

CHAPTER 7

Future Work

There are several directions for further work with respect to scarf angle research. The first would be to analyze the micro-structure of scarf-joints to determine how scarf angle affects the size and grain structure of the weld zones. A Vickers hardness testing machine would have fine enough precision to exactly determine the size and dimensions of the weld zones. Although a similar analysis was considered for this study the only available equipment was a Rockwell Hardness tester, which lacks the necessary precision required for quantifying zone dimensions with hardness values.

The results of a preliminary study with 30° scarf joints showed that a pin offset could be used to achieve sound quality welds, meaning that tenable scarf angles are not constrained by the relationship posited by Sethi et al. [16] in equation (2.1), which was shown valid for only centered pin alignments. Future work would involve a parameter study of the effect of pin offsets for low scarf angles on weld quality. This could potentially introduce a process optimization, or at least establish a criterion for determining tenable scarf joint configurations for low scarf angles.

An additional area which could be pursued would be to study the relationship between plate thickness and pin geometry on scarf weld quality. This study sought to isolate for the effect of surface angle on weld characteristics specifically for quarter-inch material. However, the comparison between the results of this study and those of Sethi et al. suggests that the constraints for scarf angle could potentially depend more on the relationships between pin diameter, pin-length, and plate thickness. Such a parameter study could develop a criterion for better determining tenable joint configurations based on the dimensions of the tooling and material utilized.

References

- [1] R. S. Mishra and Z. Y. Ma, "Friction stir welding and processing," *Materials Science and Engineering R: Reports*, vol. 50, no. 1–2, Aug. 31, 2005. doi: 10.1016/j.mser.2005.07.001.
- [2] M. K. Kulekci, U. Esme, and B. Buldum, "Critical analysis of friction stir-based manufacturing processes," *International Journal of Advanced Manufacturing Technology*, vol. 85, no. 5–8, pp. 1687–1712, Jul. 2016, doi: 10.1007/s00170-015-8071-5.
- [3] L. E. Murr, "A review of FSW research on dissimilar metal and alloy systems," *Journal of Materials Engineering and Performance*, vol. 19, no. 8, pp. 1071–1089, Nov. 2010, doi: 10.1007/s11665-010-9598-0.
- [4] D. Jacquin and G. Guillemot, "A review of microstructural changes occurring during FSW in aluminium alloys and their modelling," *Journal of Materials Processing Technology*, vol. 288. Elsevier Ltd, Feb. 01, 2021. doi: 10.1016/j.jmatprotec.2020.116706.
- [5] B. T. Gibson et al., "Friction stir welding: Process, automation, and control," *Journal of Manufacturing Processes*, vol. 16, no. 1, pp. 56–73, Jan. 2014, doi: 10.1016/j.jmapro.2013.04.002.
- [6] S. Muthukumaran and S. K. Mukherjee, "Multi-layered metal flow and formation of onion rings in friction stir welds," *International Journal of Advanced Manufacturing Technology*, vol. 38, no. 1–2, pp. 68–73, Jul. 2008, doi: 10.1007/s00170-007-1071-3.
- [7] "Friction Stir Welding - TWI." <https://www.twi-global.com/technical-knowledge/job-knowledge/friction-stir-welding-147> (accessed Feb. 6th, 2022).
- [8] S. Emamian et al., "A review of friction stir welding pin profile," *Lecture Notes in Mechanical Engineering*, pp. 1–18, 2017, doi: 10.1007/978-981-10-4232-4_1.
- [9] W. R. Longhurst et al., "Development of friction stir welding technologies for in-space manufacturing," *International Journal of Advanced Manufacturing Technology*, vol. 90, no. 1–4, pp. 81–91, Apr. 2017, doi: 10.1007/s00170-016-9362-1.
- [10] A. Arora, A. De, and T. Debroy, "Toward optimum friction stir welding tool shoulder diameter," *Scripta Materialia*, vol. 64, no. 1, pp. 9–12, Jan. 2011, doi: 10.1016/j.scriptamat.2010.08.052.
- [11] M. M. Abd Elnabi, A. B. Elshalakany, M. M. Abdel-Mottaleb, T. A. Osman, and A. el Mokadem, "Influence of friction stir welding parameters on metallurgical and mechanical properties of dissimilar AA5454-AA7075 aluminum alloys,"

Journal of Materials Research and Technology, vol. 8, no. 2, pp. 1684–1693, Apr. 2019, doi: 10.1016/j.jmrt.2018.10.015.

- [12] W. T. Evans, B. T. Gibson, J. T. Reynolds, A. M. Strauss, and G. E. Cook, “Friction Stir Extrusion: A new process for joining dissimilar materials,” *Manufacturing Letters*, vol. 5, pp. 25–28, Aug. 2015, doi: 10.1016/j.mfglet.2015.07.001.
- [13] U. Acharya et al., “A study on the implication of modified joint configuration in friction stir welding,” *Soldagem e Inspecao*, vol. 26, p. NA, 2021, doi: 10.1590/0104-9224/si26.07.
- [14] U. Kumar, U. Acharya, S. C. Saha, and B. S. Roy, “Microstructure and mechanical property of friction stir welded Al-Mg joints by adopting modified joint configuration technique,” in *Materials Today: Proceedings*, 2019, vol. 26, pp. 2083–2088. doi: 10.1016/j.matpr.2020.02.450.
- [15] P. Goel et al., “Investigation on the effect of tool pin profiles on mechanical and microstructural properties of friction stir butt and scarf welded aluminium alloy 6063,” *Metals*, vol. 8, no. 1, Jan. 2018, doi: 10.3390/met8010074.
- [16] D. Sethi, U. Acharya, S. Shekhar, and B. S. Roy, “Applicability of unique scarf joint configuration in friction stir welding of AA6061-T6: Analysis of torque, force, microstructure and mechanical properties,” *Defence Technology*, 2021, doi: 10.1016/j.dt.2021.03.010.
- [17] D. Sethi, U. Acharya, S. Kumar, S. Shekhar, and B. S. Roy, “Effect of Reinforcement Particles on Friction Stir Welded Joints with Scarf Configuration: an Approach to Achieve High Strength Joints,” *Silicon*, 2021, doi: 10.1007/s12633-021-01430-8.
- [18] Standard test method for tension testing of metallic materials. West Conshohocken, PA: ASTM International, 2016.
- [19] P. Upadhyay and A. P. Reynolds, “Effects of thermal boundary conditions in friction stir welded AA7050-T7 sheets,” *Materials Science and Engineering A*, vol. 527, no. 6, pp. 1537–1543, Mar. 2010, doi: 10.1016/j.msea.2009.10.039.
- [20] R. Abbaschian, L. Abbaschian, and R.E. Reed-Hill, “Physical Metallurgy Principles”, 4th edition, Samford CT, Cengage Learning, 2008, pp 700-706.
- [21] S. Hassanifard, H. Alipour, A. Ghiasvand, and A. Varvani-Farahani, “Fatigue response of friction stir welded joints of Al 6061 in the absence and presence of inserted copper foils in the butt weld,” *Journal of Manufacturing Processes*, vol. 64, pp. 1–9, Apr. 2021, doi: 10.1016/j.jmapro.2021.01.010.

Appendix A

Appendix

Figures(A.1–A.13) represent the raw tensile test data acquired from the Instron tensile tester. As the macroscopic properties of UTS were the goal of the testing an extensometer was not used. This is why these elongation data were not utilized in the analysis.

Width and thickness dimensions of the dog bone samples prepared for tensile testing are presented in Table(A.1). The width dimension recorded is the average width of the dog bone test section, which was relatively uniform with small variations. Thickness measurements taken were meant to allow for thickness to be interpolated if necessary depending on failure location. The mid-thickness is sometimes less than that of the edges due to material extrusion. However, the thickness at the AS and RS are representative of the base plate thickness, which can be seen to have significant variation around the nominal thickness of 0.25-in.

Table(A.2) provides the weld sample widths before welds were conducted. The majority are below the nominal 4-in width due to prep of the faying surfaces requiring material to be milled off.

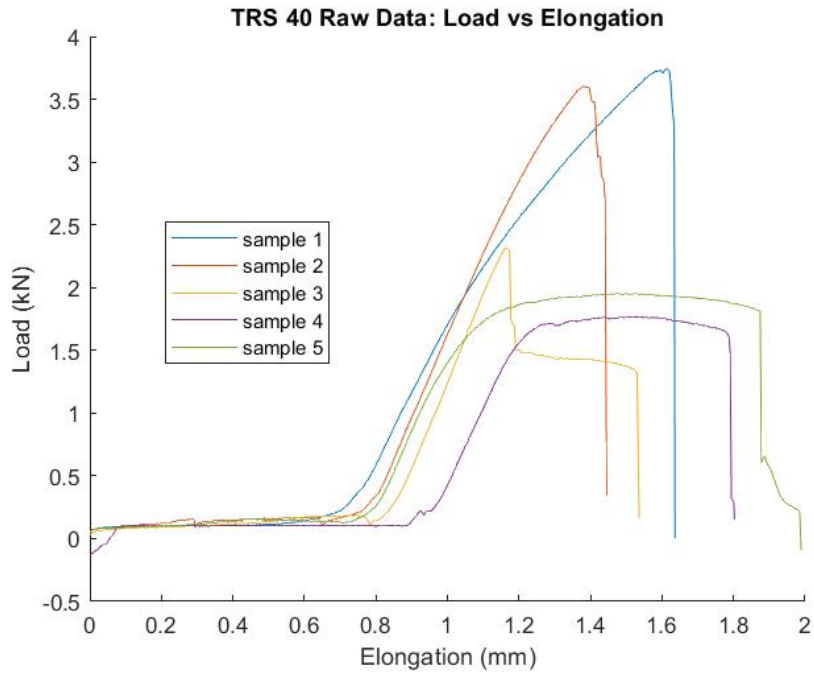


Figure A.1: Raw Load and Extension data from Tensile Testing for the TRS 40^o weld samples

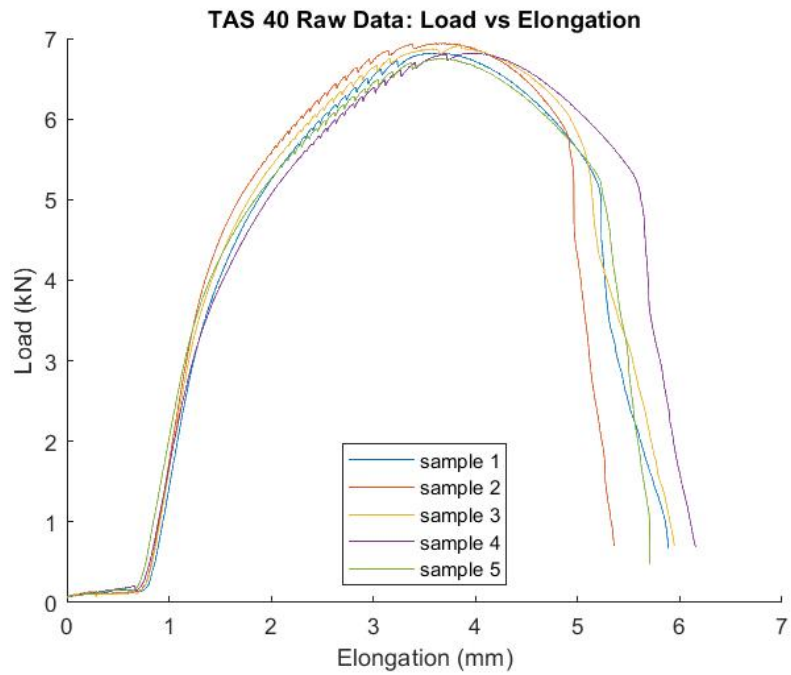


Figure A.2: Raw Load and Extension data from Tensile Testing for the TAS 40^o weld samples

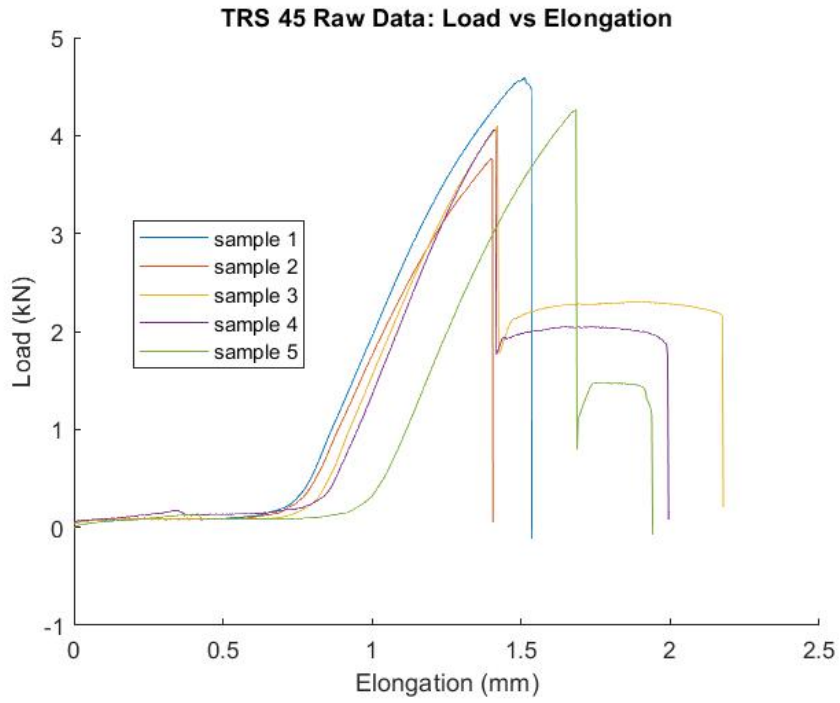


Figure A.3: Raw Load and Extension data from Tensile Testing for the TRS 45^o weld samples

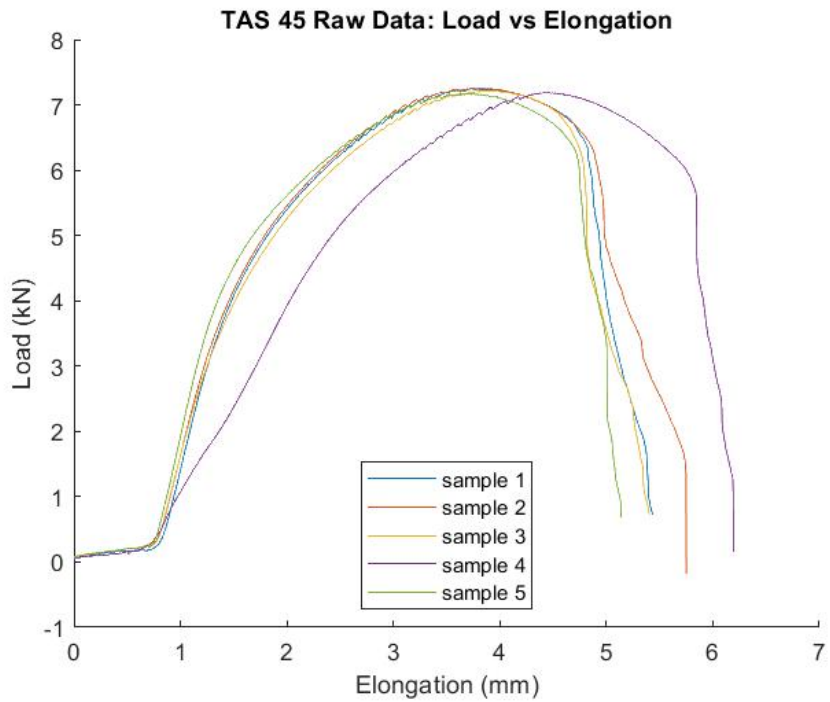


Figure A.4: Raw Load and Extension data from Tensile Testing for the TAS 45^o weld samples

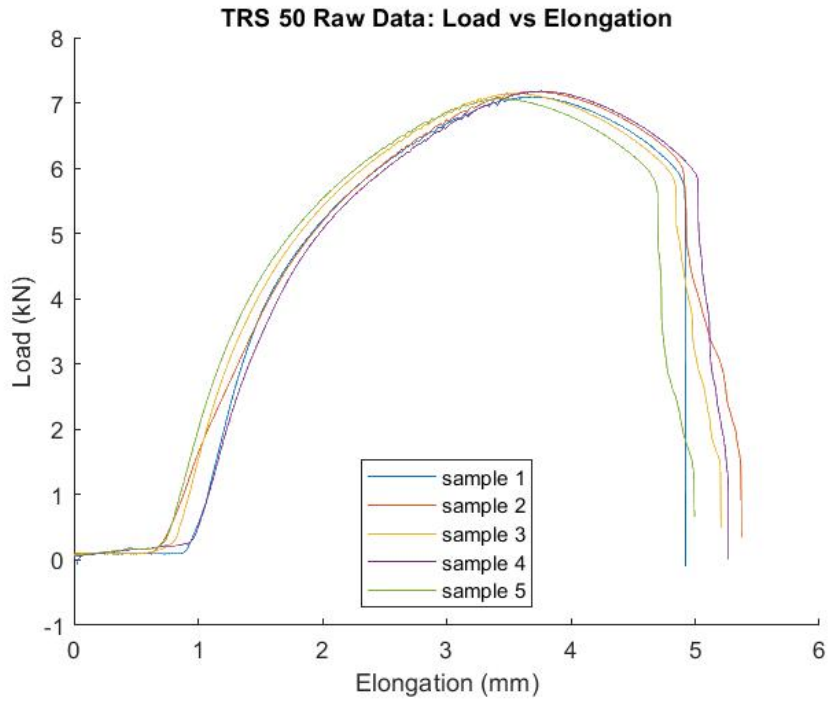


Figure A.5: Raw Load and Extension data from Tensile Testing for the TRS 50° weld samples

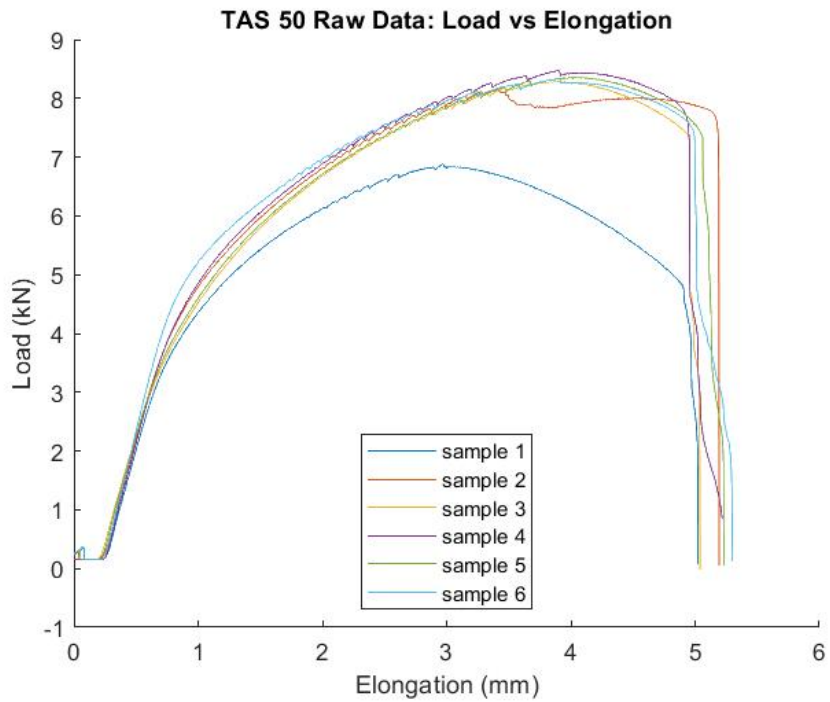


Figure A.6: Raw Load and Extension data from Tensile Testing for the TRS 50° weld samples

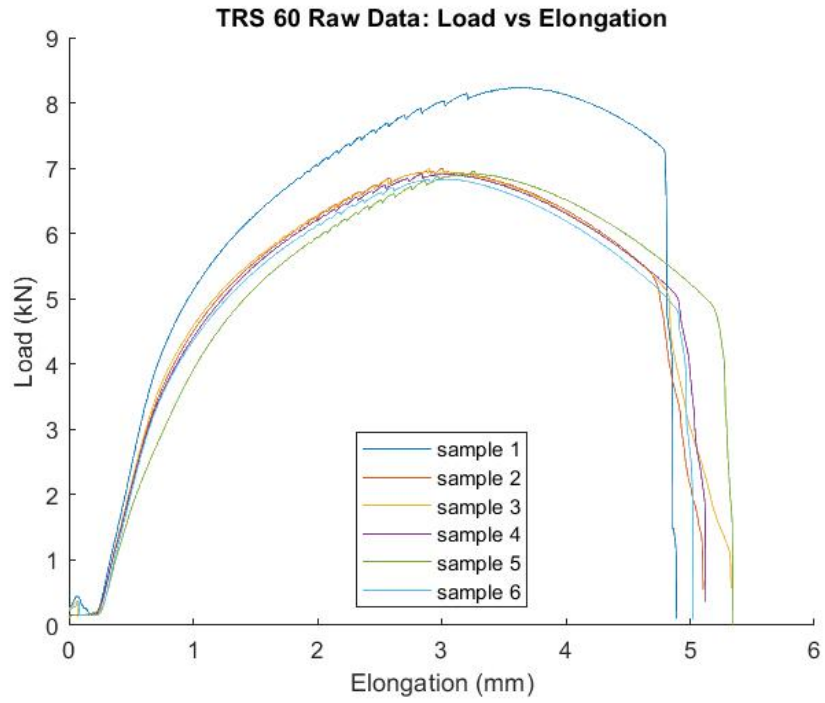


Figure A.7: Raw Load and Extension data from Tensile Testing for the TRS 60° weld samples

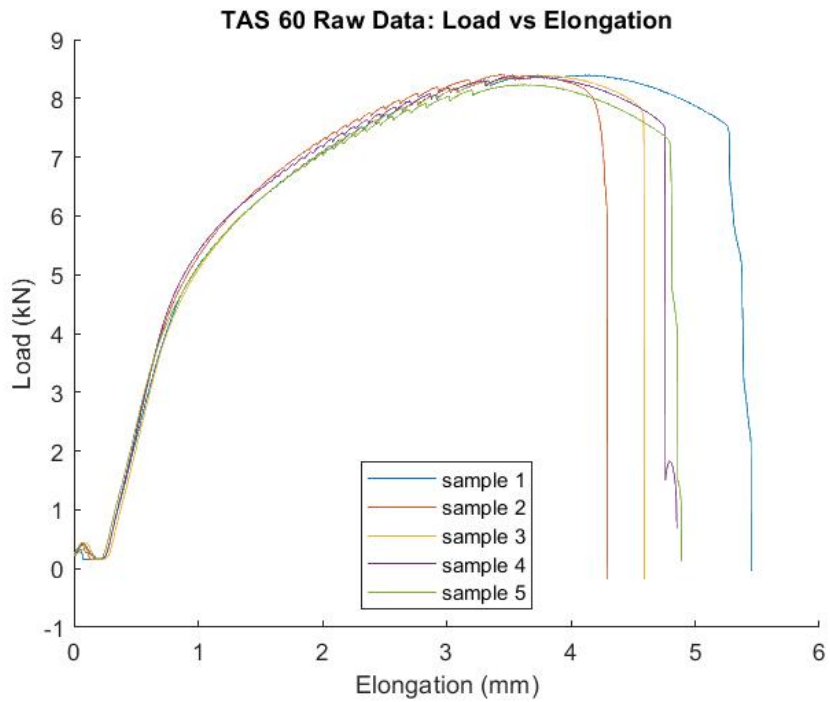


Figure A.8: Raw Load and Extension data from Tensile Testing for the TAS 60° weld samples

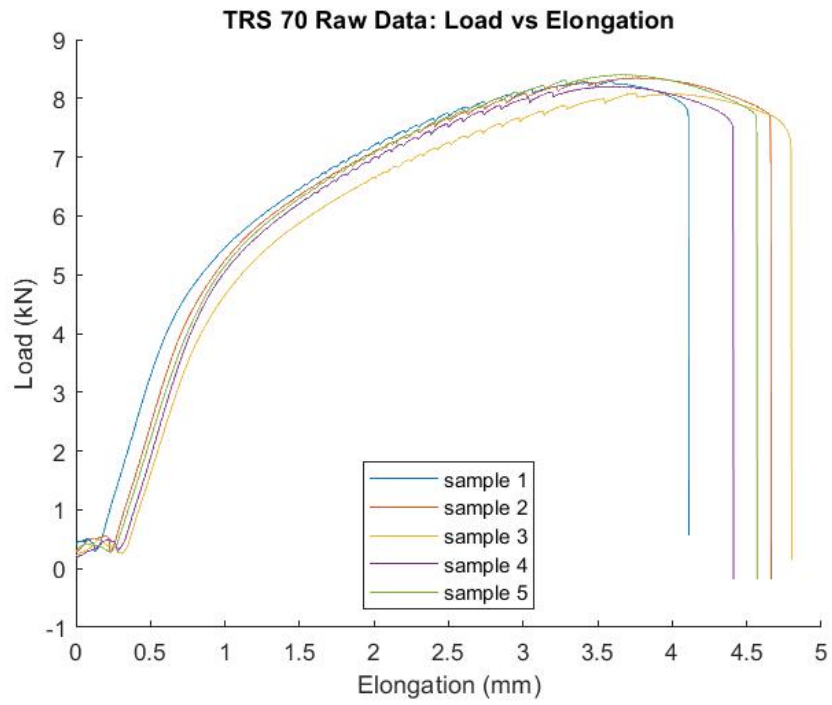


Figure A.9: Raw Load and Extension data from Tensile Testing for the TRS 70° weld samples

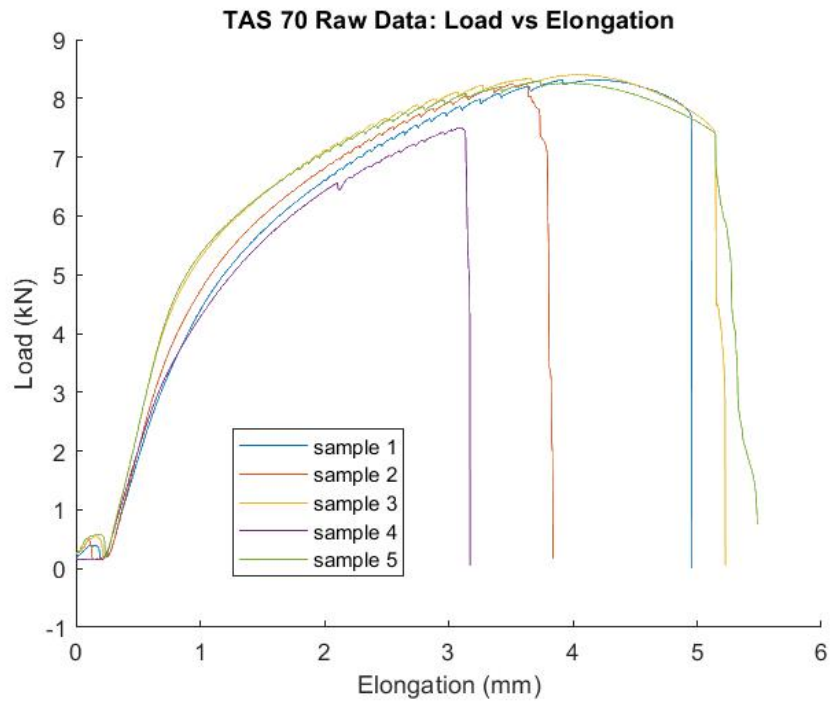


Figure A.10: Raw Load and Extension data from Tensile Testing for the TAS 70° weld samples

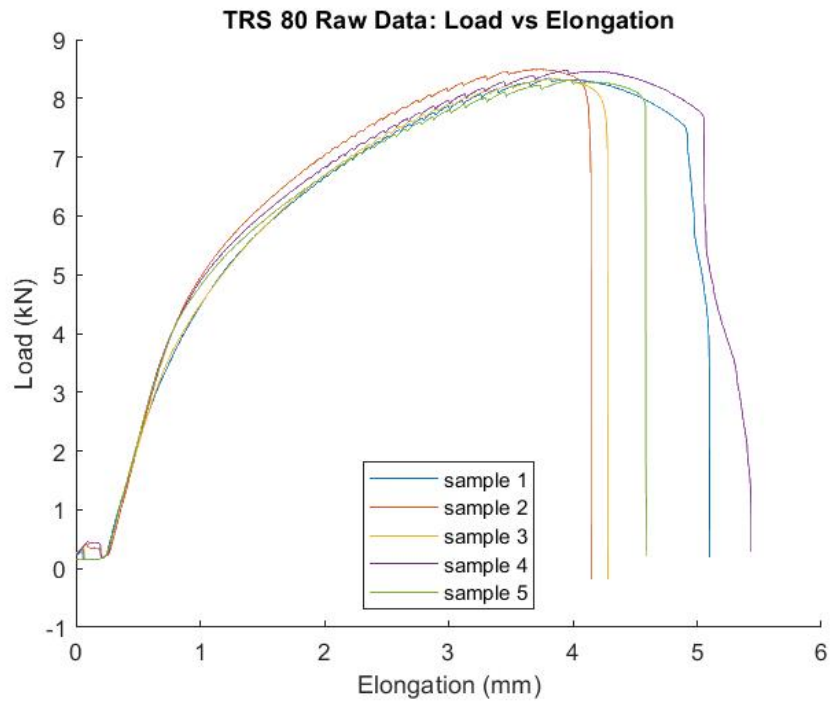


Figure A.11: Raw Load and Extension data from Tensile Testing for the TRS 80° weld samples

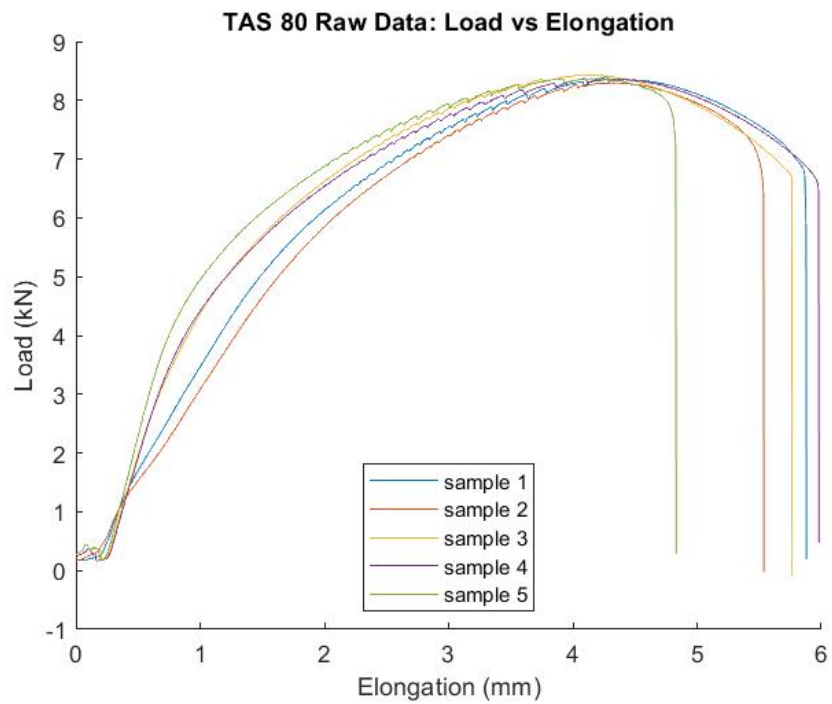


Figure A.12: Raw Load and Extension data from Tensile Testing for the TAS 80° weld samples

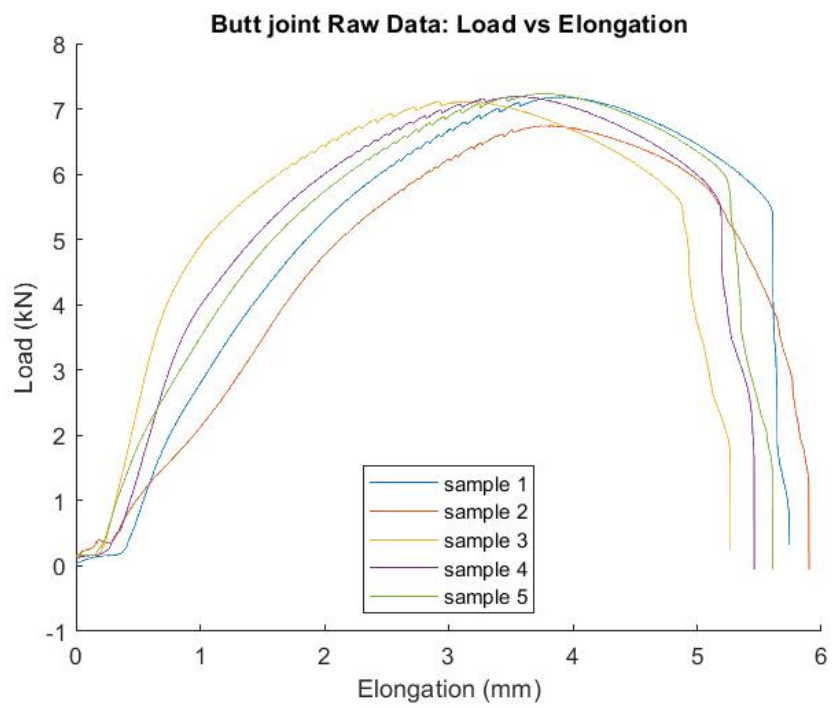


Figure A.13: Raw Load and Extension data from Tensile Testing for the butt weld samples

	Sample #	Mid Thickness (in)	RS Thickness (in)	AS thickness (in)	width (in)	CA (in ²)	CA (m ²)
Butt	1	0.251	0.258	0.259	0.252	0.0633	4.081E-05
	2	0.251	0.263	0.260	0.251	0.0630	4.065E-05
	3	0.249	0.265	0.264	0.253	0.0630	4.064E-05
	4	0.248	0.261	0.260	0.252	0.0625	4.032E-05
	5	0.253	0.262	0.262	0.251	0.0635	4.097E-05
TAS 80	1	0.252	0.261	0.262	0.254	0.0640	4.130 E-05
	2	0.248	0.261	0.260	0.250	0.0619	3.992E-05
	3	0.251	0.259	0.260	0.249	0.0625	4.032E-05
	4	0.249	0.257	0.261	0.252	0.0628	4.048E-05
	5	0.254	0.260	0.258	0.251	0.0638	4.113E-05
TRS 80	1	0.247	0.251	0.253	0.249	0.0615	3.968E-05
	2	0.251	0.245	0.252	0.253	0.0635	4.097E-05
	3	0.246	0.249	0.251	0.256	0.0630	4.063E-05
	4	0.251	0.252	0.249	0.248	0.0622	4.016E-05
	5	0.252	0.253	0.250	0.250	0.0630	4.065E-05
TAS 70	1	0.246	0.259	0.260	0.249	0.0613	3.952E-05
	2	0.251	0.257	0.259	0.248	0.0622	4.016E-05
	3	0.254	0.256	0.258	0.250	0.0635	4.097E-05
	4	0.255	0.262	0.260	0.252	0.0643	4.146E-05
	5	0.254	0.260	0.260	0.250	0.0635	4.097E-05
TRS 70	1	0.2535	0.256	0.260	0.244	0.0619	3.991E-05
	2	0.254	0.258	0.256	0.250	0.0635	4.097E-05
	3	0.251	0.257	0.257	0.244	0.0612	3.951E-05
	4	0.257	0.261	0.259	0.248	0.0637	4.112E-05
	5	0.26	0.258	0.257	0.250	0.0650	4.194E-05
TAS 60	1	0.258	0.257	0.259	0.249	0.0642	4.145E-05
	2	0.257	0.269	0.260	0.250	0.0643	4.145E-05
	3	0.258	0.265	0.264	0.249	0.0642	4.145E-05
	4	0.259	0.262	0.260	0.251	0.0650	4.194E-05
	5	0.263	0.261	0.262	0.250	0.0658	4.242E-05
TRS 60	1	0.248	0.254	0.244	0.250	0.0620	4.000E-05
	2	0.257	0.250	0.253	0.250	0.0643	4.145E-05
	3	0.251	0.248	0.250	0.249	0.0625	4.032E-05
	4	0.248	0.246	0.249	0.250	0.0620	4.000E-05
	5	0.245	0.245	0.254	0.251	0.0615	3.967E-05
TAS 50	1	0.253	0.255	0.265	0.250	0.0633	4.081E-05
	2	0.255	0.262	0.256	0.252	0.0643	4.146E-05
	3	0.256	0.258	0.258	0.250	0.0640	4.129E-05
	4	0.255	0.259	0.259	0.250	0.0638	4.113E-05
	5	0.254	0.259	0.260	0.253	0.0643	4.146E-05
TRS 50	1	0.249	0.244	0.257	0.251	0.0625	4.032E-05
	2	0.25	0.245	0.263	0.250	0.0624	4.020E-05
	3	0.246	0.258	0.263	0.250	0.0614	3.960E-05
	4	0.248	0.245	0.256	0.250	0.0619	3.992E-05
	5	0.2465	0.254	0.257	0.250	0.0616	3.976E-05
TAS 45	1	0.25	0.2515	0.249	0.249	0.0623	4.016E-05
	2	0.252	0.249	0.250	0.248	0.0625	4.032E-05
	3	0.255	0.250	0.251	0.250	0.0636	4.105E-05
	4	0.259	0.250	0.249	0.250	0.0646	4.170E-05
	5	0.251	0.254	0.250	0.248	0.0623	4.016E-05
TRS 45	1	0.261	0.247	0.258	0.248	0.0647	4.176E-05
	2	0.258	0.246	0.253	0.248	0.0640	4.128E-05
	3	0.2595	0.249	0.255	0.249	0.0645	4.160E-05
	4	0.258	0.255	0.259	0.248	0.0640	4.128E-05
	5	0.261	0.262	0.260	0.249	0.0650	4.193E-05
TAS 40	1	0.246	0.246	0.247	0.250	0.0614	3.960E-05
	2	0.246	0.246	0.247	0.248	0.0610	3.936E-05
	3	0.246	0.246	0.248	0.250	0.0614	3.960E-05
	4	0.2495	0.246	0.245	0.249	0.0621	4.008E-05
	5	0.2455	0.245	0.246	0.249	0.0611	3.944E-05
TRS 40	1	0.248	0.247	0.245	0.248	0.0615	3.968E-05
	2	0.25	0.247	0.246	0.249	0.0623	4.016E-05
	3	0.249	0.249	0.247	0.248	0.0618	3.984E-05
	4	0.249	0.246	0.247	0.248	0.0618	3.984E-05
	5	0.255	0.245	0.246	0.25	0.0638	4.113E-05

Table A.1: Tensile test dog bone dimensions.

	butt	TAS	TRS	TAS	TRS	TAS	TRS
angle	90	80	80	70	70	60	60
AS (in)	2.002	1.947	1.747	1.964	1.912	1.939	1.952
RS (in)	2.003	1.891	1.691	1.932	1.858	1.953	1.965
Total (in)	4.005	3.838	3.438	3.896	3.77	3.892	3.917
Total (mm)	101.727	97.485	87.325	98.958	95.758	98.857	99.492
	TAS	TRS	TAS	TRS	TAS	TRS	X
angle	50	50	45	45	40	40	X
AS (in)	1.853	1.85	1.944	1.9545	1.991	1.967	X
RS (in)	1.859	1.859	1.939	1.855	1.985	1.958	X
Total (in)	3.712	3.709	3.883	3.8095	3.976	3.925	X
Total (mm)	94.285	94.209	98.628	96.761	100.990	99.695	X

Table A.2: Pre-weld lengths of all weld samples.